ECCOMAS Congress 2016
VII European Congress on Computational Methods in Applied Sciences and Engineering
M. Papadrakakis, V. Papadopoulos, G. Stefanou, V. Plevris (eds.)
Crete Island, Greece, 5–10 June 2016

VECTOR FIELD GUIDED TOOL PATHS FOR FIVE-AXIS MACHINING

Stanislav S. Makhanov
School of Information and Computer Technology, Sirindhorn International Institute of Technology, Thammasat University, Thailand
e-mail: makhanov@siit.tu.ac.th

Keywords: kinematics of the milling machines, error minimization, toolpath planning

Abstract. *We propose a new framework for toolpath generation for 5 axis machining of part surfaces represented by the StereoLithography (STL) format. The framework is based on flattening the STL part and generation of curvilinear toolpaths adapted to the vector field of optimal directions. The experiments show that there is no universal sequence of steps applicable to every surface. However, a correct choice of the tools available within the proposed ACT-framework always leads to a substantial improvement of the toolpath, in terms of its length and the machining time.*

1 INTRODUCTION

A milling machine is a programmable mechanism, guided by a controller fed with a CNC program (G-code) . The G-code is derived from a toolpath $\Omega = \{\Omega_0, \Omega_1, ..., \Omega_m\}$, consisting of the pairs $\Omega_p = \{M_p, I_p\}$, where $M_p = (x_p, y_p, z_p)$ is the Cartesian coordinates of the cutter location (CL) points in the machine coordinate system, and $I_p = \{I_{x,p}, I_{y,p}, I_{z,p}\}$ are the tool orientation vectors. The rotation angles, $\Re_p = (a_p, b_p)$ to control the rotary and the tilt table of the machine, are functions of the tool orientation vectors. Therefore, the toolpath can also be defined by $\Pi_M = \{\Pi_{M,0}, \Pi_{M,1}, ..., \Pi_{M,m}\}$, where $\Pi_{M,p} = \{M_p, \Re_p\}$. The Cartesian coordinates in the machine coordinates are usually derived from the corresponding toolpath in the workpiece coordinates, given by $\Pi_W = \{\Pi_{W,0}, \Pi_{W,1}, ..., \Pi_{W,m}\}$, $\Pi_{W,p} = \{W_p, \Re_p\}$, $W_p = (X_p, Y_p, Z_p) \in S(u,v)$, where $S(u,v)$ denotes the part surface and *u*,*v* the parametric coordinates. The configuration of the 5 axis milling machine is characterized by the relative positions of the rotary and linear axes, with regard to the tool and the workpiece. On a very basic level the machines can be categorized by the positions of the rotational joints as follows:

The 2-0 machine. Two rotary axes on the table.
The 1-1 machine. One rotary axis on the table and one on the tool.
The 0-2 machine. Two rotary axes on the tool.

Figures 1 and 2 display the configuration 2-0 used in this study.

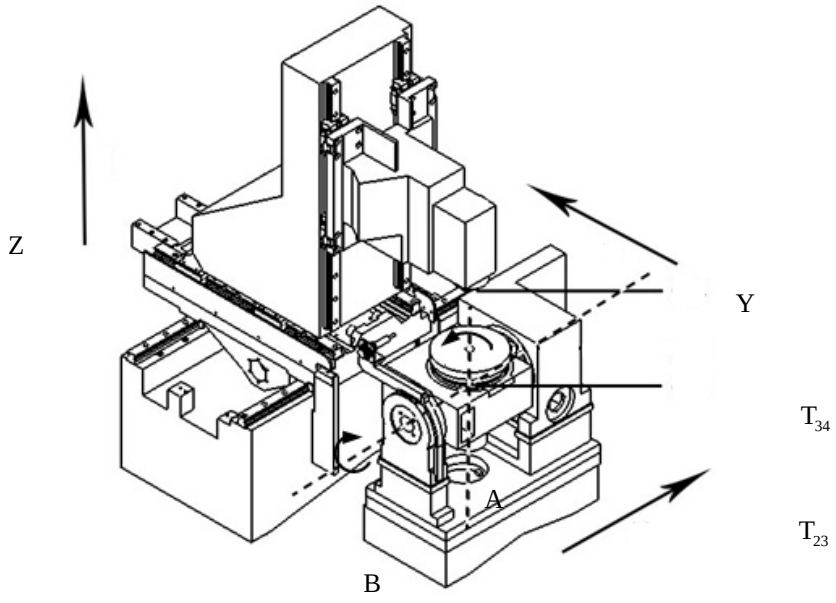

Figure 1. Five axis milling machine with rotary axes on the table

Figure 2. HAAS VF2TR

The toolpath optimization usually aims to reduce the total length of the toolpath or the total machining time, maintaining the prescribed accuracy. Alternatively, the user may wish to improve the accuracy while keeping or even reducing the machining time [1,2].

Furthermore, we differentiate the toolpath in the machine and the workpiece coordinates. In particular, our techniques account for the fact that minimization of the toolpath in the workpiece coordinates does not necessarily minimize it in the machine coordinates and does not necessarily minimize the machining time. However, optimization in the workpiece coordinates is machine independent and computationally easy. That is why the strategy to minimize the toolpath is often based on a machine independent criterion such as maximization of the machining strip [3], minimization of the scallops, etc. However, the reduction of the kinematic error and the machining time are the ultimate goals of 5–axis optimization [4-8].

Let C be the quality criterion, ε the difference between the actual and the desired tool trajectory, h the scallop height, and ε' the prescribed accuracy. The basic quality criterion is the length of the toolpath in the workpiece/machine coordinates and the machining time. Our toolpath generation employs a direct estimate of the basic criterion. It may also use another measure, which includes that criterion implicitly. For instance, instead of minimization of the length $C = L$ one can consider $C' = -R_M$ where R_M is the material removal rate or $C' = \varepsilon$, where ε is the kinematic error.

We also consider a quality criterion measure represented by a vector-function. At every point $W_p = (X_p, Y_p, Z_p)$, we evaluate an optimal direction (vector), using one of the above scalar criteria. The collection of these vectors constitutes the target vector field denoted by V.

The optimization problem is then given by

$$\underset{\Pi_W}{\text{minimize}}\, \text{dist}(V, V_W)$$

$$\text{subject to}$$

$$\varepsilon_p \le \varepsilon',$$

$$h_p \le \varepsilon',$$

where dist denotes an appropriate distance, and $V_W = \bigcup_{p=0}^{m-1} W_p \overrightarrow{W}_{p+1}$ is the desired vector field.

Although V and C' are not related explicitly, we will show that the solution of the above optimization problem minimizes or at least reduces C' and consequently C.

Originally, the toolpath relative to a certain vector field was proposed in [9,10] and iso-scallop toolpaths in [1]. In [3], the part surface is covered by potential machining patches characterized by the optimal directions, corresponding to the maximum machining strip. The vector field of the optimal tool directions, to capture the "skeletal" information of toolpath (or a family of a toolpaths), was combined with the geometric constraints, and the kinematic performance of the machine and other constraints were evaluated such as the cutting force limits in [11,12]. The part surface was partitioned into clusters so that the streamlines of the vector field are close to the conventional isoparametric (ISO) or spiral in [13,14]. Optimal or nearly optimal directions can be combined with rear gouging, global gouging, and machine limits constraints [15]. Recently a machine-dependent vector field has been proposed in [43]. However, all the above algorithms construct the toolpath by offsetting an initial path and propagating the offsets inside the region. When the offset deviates from the optimal directions the algorithm requires a new initial track. Such strategies are usually sensitive to small variations of the optimization criterion. Moreover, finding the initial toolpath is a computationally expensive, NP hard problem. Additional efforts must be made to ensure that the resulting toolpath is structured and not self-intersecting.

In [16], we construct a curvilinear toolpath aligned with the optimal vector field using the elliptic grid generation. The optimal directions are evaluated using the maximum material removal rate. The proposed vector field aligned path (ACT) is a compromise between the flexibility of methods based on propagating of the initial track and the simplicity of the ISO topology. The method extends scalar based grid generation for five-axis machining originally proposed in [17,14,18-21] and independently in [22].

The flexibility of grid generation methods makes it possible to use a variety of cost functions and boundary adapted grids and domain decomposition methods. Although these options are well known in computational hydro and aerodynamics, they have not been fully exploited in the framework of five-axis machining. Furthermore, the toolpath can be further improved by applying the space filling curves (SFC) [23,24] and the biased space filling curves (BSFC) [16].

An important practical application of the toolpath generation methods is machining surfaces represented by the STL format. In order to apply the ACT to the STL surfaces, we have to either adapt the algorithms to the 3D case or flatten the STL surface and generate the required curvilinear grid in the resulting parametric domain. Noting that meshing algorithms

in 2D are more efficient than in 3D [25] , we incorporate a “radial plane” flattening approach into the proposed framework (see the forthcoming section Flattening Algorithm).
Our methodology includes the following components:

1. Flattening.
2. Evaluation of the surface characteristics in the parametric domain.
3. Grid generation in the parametric domain.
   3.1.1 Boundary fitted grids.
   3.1.2 Different types of grids, such as the C-grid, O-grid, H-grid [26].
   3.1.3 Grids adapted to control functions: scalar functions, vector fields.
4. Space filling curves
   4.1 Adaptive space filling curves.
   4.2 Biased space filling curves.

The methodology has been tested on a variety of STL surfaces, including surfaces with multiple ridges, human masks, as well as dental crowns or even tooth implants represented by the STL files. In particular, we demonstrate the efficiency of the algorithms by machining all types of human teeth: molars, premolars, canines, and incisors. The proposed tools have been tested against the standard ISO path, MasterCam generated path, and advanced toolpath generation methods of NX9. The tools available within the ACT-framework are capable of substantially improving the quality of the toolpath, in terms of its length, the machining time and the kinematic error.

2 FLATTENING ALGORITHM

The majority of toolpath generation techniques have been demonstrated on a single parametric surface, such as the Bezier patch, Gregory patch, B-spline, etc. However, the explicit parametric representation is rarely used in the industry. The most popular formats are STL [27], IGES [28], STEP [29], SET [30], CATIA [31], and PHIGS [32]. The STL format, which approximates the surface of a solid model by triangles, is becoming the standard for the rapid prototyping industry and is increasingly popular in multi-axis manufacturing. The main reason is its simplicity and applicability to an arbitrary surface. The algorithms for flattening triangulated or tessellated surfaces have been used in many research areas, such as generation of clothing patterns, 3D reconstruction, texture mapping reconstruction, multiresolutional analysis, formation of ship hulls, metal forming, etc. By flattening, we understand a one-to-one mapping of the STL surface to a planar domain in the parametric space. Geometrically, the flattening algorithm unfolds the surface onto a plane without self-intersections, that is, each point of the original surface is associated with a unique point (u,v) in the parametric space. A variety of algorithms have been proposed for parameterization of the triangulated surfaces[33]-[39]. In this paper we propose radial plane flattening and demonstrate that it works for a particular practical case of STL surfaces representing human teeth. The method was also successfully tested on parts which can be roughly approximated by surfaces having radial symmetry. Note that this approximation could be very far from ideal, however, radial flattening still works better than some general commercial software. Besides, the proposed algorithm preserves distances along the trajectories in the radial planes and reduces angular and metric distortions in the proximity of the focus point [40].
We define a polar coordinate system centered at a point of reference O_p. Given the surface’s tangential plane at the reference point, a perpendicular plane through the reference point, and an arbitrary STL point S', we evaluate the trajectory connecting O_p and S' on

the surface by finding intersections of the radial plane and the corresponding STL triangles (Figure 3).

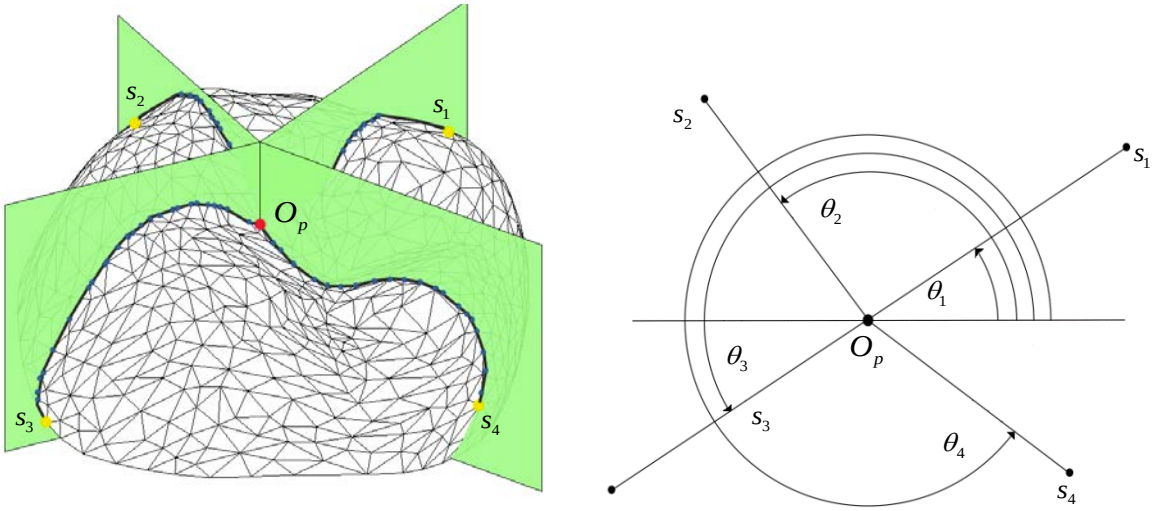

(a) (b)

Figure 3. Radial plane flattening algorithm

The technique requires solving a large series of linear (possibly singular) systems, 2x2 and 3x3, and a special tracing procedure to connect the intersection points.

The new coordinates (s,θ) are the length of the trajectory $O_p\,S'$ and the angle between the radial plane and the reference plane, respectively (Figure 3). Note that the radial flattening does not necessarily mean that the curvilinear grid must be polar. As a matter of fact, we map the resulting triangles onto the Cartesian plane. However, using a polar parametrization and the spiral toolpath is a feasible option which can be implemented by the ACT as well. Figure 4 compares the proposed algorithm with MeshFlatten [41].

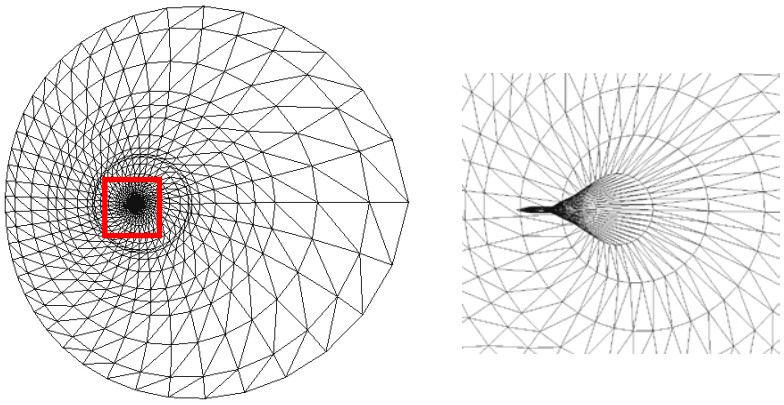

(b) (c)

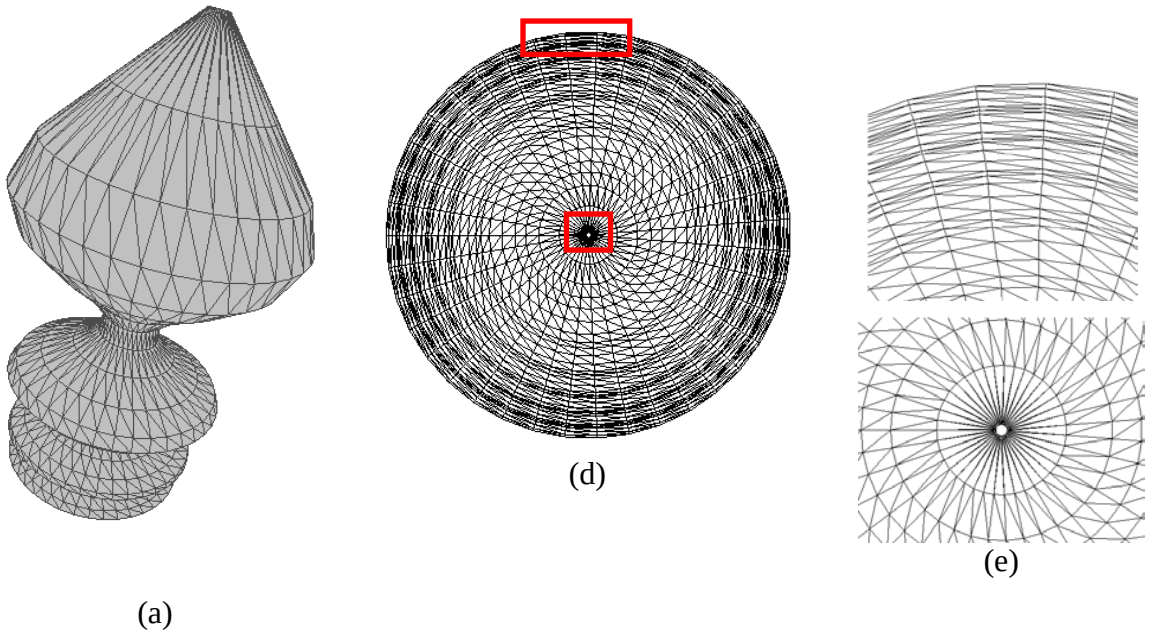

(a) (d) (e)

Figure 4. Flattening (a) 3D Model (b)-(c) MeshFlatten, (d)-(e) radial plane flattening

Clearly, MeshFlatten fails to return an acceptable parametrization, whereas a correct choice of the reference point O_p allows for construction of the required flattening using the proposed approach.

3 MATERIAL REMOVAL RATE

Let W_1 be an arbitrary cutter contact (CC) point on the surface (see [7] regarding the relationship between the CC and CL points). Consider a disk defined by $\Omega_{W_1} = \{W : \mathrm{dist}(W_1, W) = l_1\}$, where dist denotes an appropriate distance on the surface, and l_1 is an arbitrary step (see Figure 5). The corresponding disk in the machine coordinates is denoted by Ω_{M_1}. The distance between the center of the disk M_1 and the points belonging to Ω_{W_1} is given by $l_{1,M} \equiv l_{1,M}(W)$.

The machining strip along the feed direction $\vec{W_1, W}$ is denoted by $w_1 \equiv w_1(W)$. It is evaluated by locating the intersections of the effective cutting shape and the part surface [24].

Our target vector at W_1 is defined as $\vec{W_1, W_2}$, where $W_2 = \arg\max_{W \in \Omega_{W_1}} C_1'(W)$, and where $C_1'(W) = w_1(W)$, $C_1'(W) = l_{1,M}(W)$ or $C_1'(W) = R_{1,M}(W)$, where $R_{1,M}(W)$ denotes the material removal rate (MRR) . In order to define the MRR, assume that only the rotation axes can exceed the machine speed limit and that the workpiece is machined with the maximum linear speed allowed for the particular material. These assumptions are usually correct for relatively small parts, exemplified in our forthcoming section “Numerical Examples and Cutting Experiments”, where the largest blank workpiece is 100x100x100mm. In this case the required machining time is evaluated by

$t = \max(t_a, t_b)$,

where $t_a = \frac{a - a_1}{v_{a,\max}}$, $t_b = \frac{b - b_1}{v_{b,\max}}$ and, where $v_{a,\max}, v_{b,\max}$ are the maximal speeds of the rotational axes a and b, respectively.

The actual rotation speed is given by

$$v_a = \frac{a - a_1}{t},\ v_b = \frac{b - b_1}{t}.$$

Note that if $a = a_1$ and $b \neq b_1$, then $v_a = 0$. If $b = b_1$ and $a \neq a_1$, then $v_b = 0$.

If $a = a_1$ and $b = b_1$, then the maximum linear speed is allowed in each of the linear axis. Consequently, the feed rate $F = \frac{l_1}{t}$, whereas the effective MRR is evaluated by $R_M = Fw_1(W)$, where $w_1(W)$ is the corresponding machining strip.

We call the direction $W_1, \vec{W}_2$ optimal, if W_2 maximizes the cost function C_1'. Evaluating vectors $W_1, \vec{W}_2$ for each surface point and transferring them into the parametric domain (u, v) generates a discrete version of the optimal vector field, $V(u,v) \equiv (v_x(u,v), v_y(u,v))$. Following $V(u,v)$ at every CC point generates an optimal tool path. However, constructing such a tool path is not always possible. Therefore, the next section presents a vector field aligned path which is nearly optimal on a set of paths topologically similar to a Cartesian zigzag.

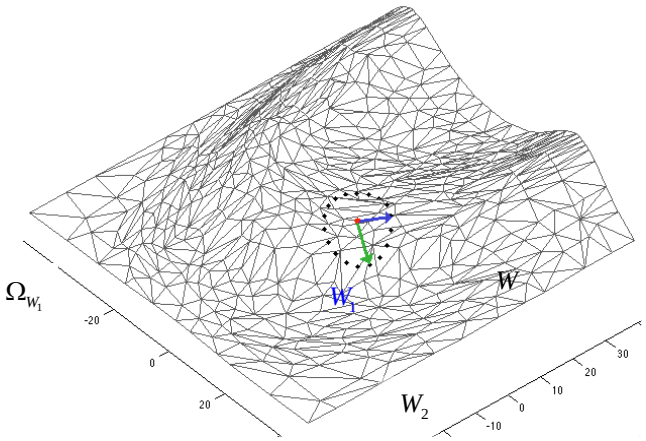

Figure 5. Material removal rate: possible directions in the workpiece coordinates

4 CURVILINEAR TOOL PATH

Recall that $S(u,v) \equiv (x(u,v), y(u,v), z(u,v))$ is the part surface, where u and v are the parametric variables. Let us consider the CC points $\{(u_{i,j}, v_{i,j}),\ 0 \le i \le N_\xi\ \ 0 \le j \le N_\eta\}$ arranged as a curvilinear grid. In other words, the CC points are a discrete analogy of a mapping $\{u(\xi,\eta), v(\xi,\eta)\}$ from the computational region $\Delta = \{0 \le \xi \le N_\xi,\ 0 \le \eta \le N_\eta\}$ onto a physical region K in the parametric coordinates u, v. In other words, the rectangular grid $\{(i, j), 0 \le i \le N_\xi\ \ 0 \le j \le N_\eta\}$ being fed to $\{u(\xi,\eta), v(\xi,\eta)\}$ becomes $\{u_{i,j}, v_{i,j}\}$ (see Figure 6).

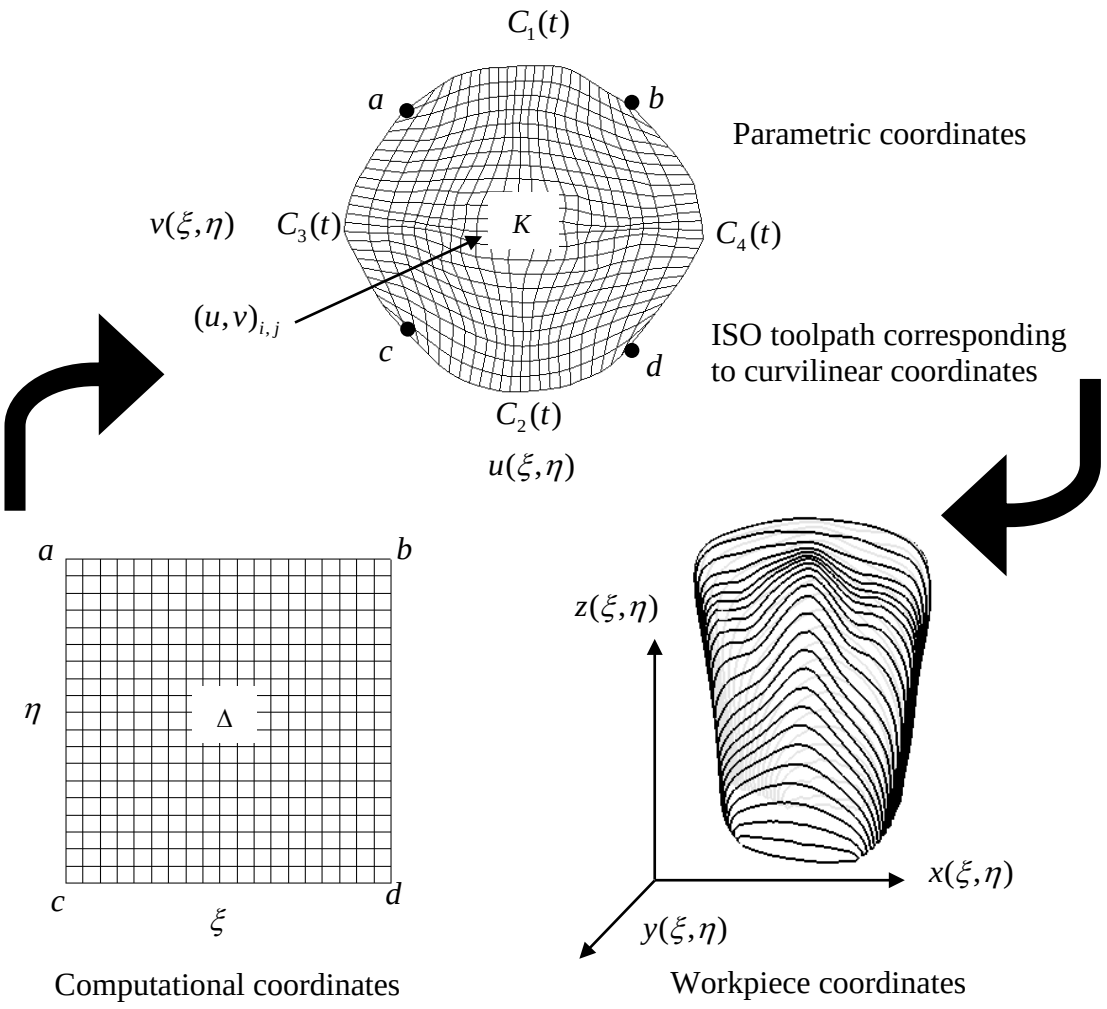

Figure 6. Coordinate transformations and the curvilinear grids, Δ denotes the computational domain, *K* the parametric domain

We adapt the curvilinear grid to the boundary of the parametric domain obtained by flattening. Furthermore, we consider adaptation to the vector field $V(u,v)$ using a modification of classical grid generation methods [20] as follows:

The smoothness of the grid is controlled by a variational functional given by

$$F_S = \int\int u_\xi^2 + u_\eta^2 + v_\xi^2 + v_\eta^2 \mathrm{d}\xi\mathrm{d}\eta \ , \tag{1}$$

where subscripts denote the partial derivatives.

Furthermore, the idea of a curvilinear grid adapted to the vector field is borrowed from computational fluid dynamics where such grids were exploited to improve the accuracy of the numerical solution of partial differential equations [44-46]. Consider a vector field $V(u,v)$ derived from a cost function C' (machining strip, length of the toolpath, material removal rate, see the previous section). Furthermore, we partition $V(u,v)$ into a dual vector field $V_D(u,v) = (\alpha(u,v),\beta(u,v))$, corresponding to the ξ and η directions as follows:

$$\alpha(u,v) = \begin{cases} V(u,v) \in \Omega_\xi, \\ 0, \text{otherwise}, \end{cases} \quad \beta(u,v) = \begin{cases} V(u,v) \in \Omega_\eta, \\ 0, \text{otherwise}, \end{cases} \tag{2}$$

where Ω_ξ, Ω_η are prescribed subsets of $V(u,v)$ selected according to a certain criterion. For instance, if the vector field has two major directions d_ξ and d_η, the partition is performed as follows (Figure 7).

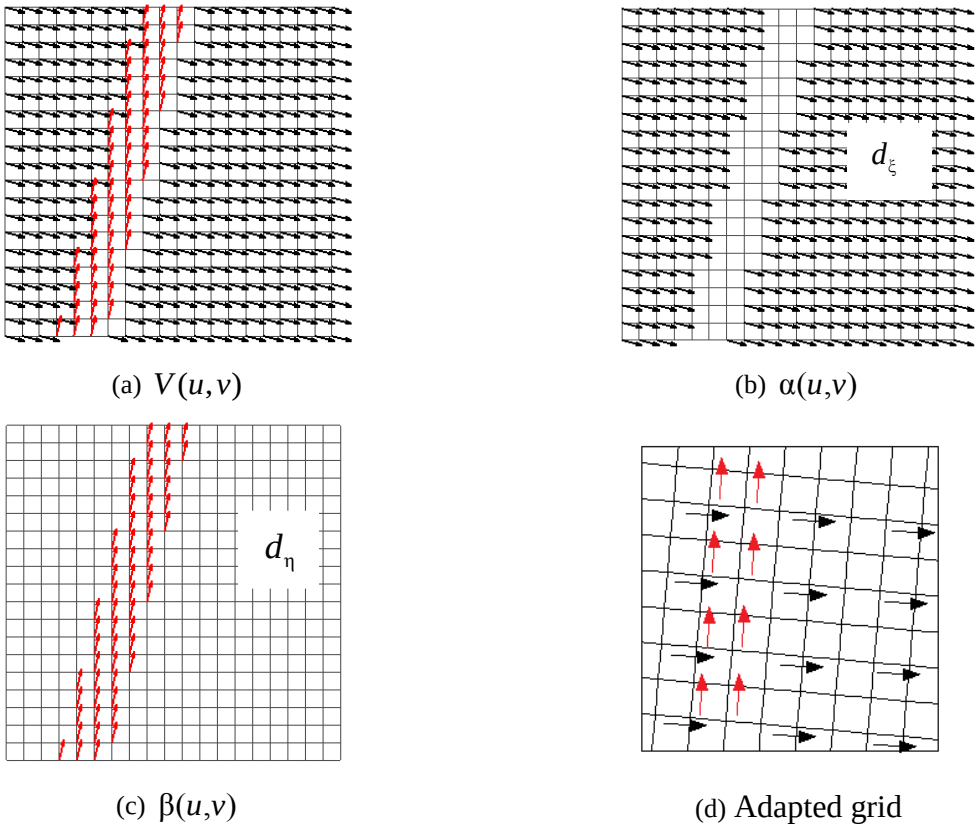

(a) $V(u,v)$ (b) $\alpha(u,v)$

(c) $\beta(u,v)$ (d) Adapted grid

Figure 7. Partition of the vector field $V(u,v)$ into $(\alpha(u,v),\beta(u,v))$

$$\alpha(u,v)=\begin{cases}\measuredangle(V,d_\xi)\approx 0 \text{ or } \measuredangle(V,d_\xi)\approx\pi,\\ 0, \quad \text{otherwise,}\end{cases}, \quad \beta(u,v)=\begin{cases}\measuredangle(V,d_\eta)\approx 0 \text{ or } \measuredangle(V,d_\eta)\approx\pi\\ 0, \quad \text{otherwise.}\end{cases}$$

The vectors from $V(u,v)$ are included into the $V_D(u,v)$ if they are almost parallel or almost anti-parallel to d_ξ or d_η. In other words, $\left|\frac{(V,d)}{\|V\|\,\|d\|}\right|-1\le\varepsilon_V$, where ε_V is the prescribed threshold.

The curvilinear grid is aligned with $V_D(u,v)$, using a modification of the grid generation techniques [44-46]. Let us align the family of the grid lines η=const with the vector field $\alpha(\xi,\eta)\equiv(\alpha_1(\xi,\eta),\alpha_2(\xi,\eta))$, whereas the grid lines ξ=const are aligned with $\beta(\xi,\eta)\equiv(\beta_1(\xi,\eta),\beta_2(\xi,\eta))$. The alignment is performed by minimizing a functional given by

$$F_V=\int\int(s_\xi\alpha')^2+(s_\eta\beta')^2\,d\xi d\eta, \tag{3}$$

where $\alpha'(\xi,\eta) \equiv (\alpha_1', \alpha_2') = (-\alpha_2, \alpha_1)$ is the vector field perpendicular to $\alpha(\xi,\eta)$, $\beta'(\xi,\eta) \equiv (\beta_1', \beta_2') = (-\beta_2, \beta_1)$ is the vector field perpendicular to $\beta(\xi,\eta)$, $s_\xi = (u_\xi, v_\xi)$, and $s_\eta = (u_\eta, v_\eta)$

Following [44], we combine the functionals F_S and F_V linearly as follows $\Phi = F_S + \lambda F_V$, where λ is the weighting coefficient.

The Euler equations are

$$\Phi_u - \Phi_{\xi,u_\xi} - \Phi_{\eta,u_\eta} = 0,$$
$$\Phi_v - \Phi_{\xi,v_\xi} - \Phi_{\eta,v_\eta} = 0.$$

Substitution $s_\xi \alpha' = u_\xi \alpha_1' + v_\xi \alpha_2'$, $s_\eta \beta' = u_\eta \beta_1' + v_\eta \beta_2'$ and differentiation yields

$$u_{\xi\xi} + u_{\eta\eta} + 2\lambda\{[\alpha_1'(\alpha_1' u_\xi + \alpha_2' v_\xi)]_\xi + [\beta_1'(\beta_1' u_\eta + \beta_2' v_\eta)]_\eta = 0, \quad (4)$$
$$v_{\xi\xi} + v_{\eta\eta} + 2\lambda\{[\alpha_2'(\alpha_1' u_\xi + \alpha_2' v_\xi)]_\xi + [\beta_2'(\beta_1' u_\eta + \beta_2' v_\eta)]_\eta = 0.$$

Furthermore, the problem can be simplified by following the optimal directions only where the alignment with the vector field leads to a significant reduction of the cost function. Therefore, the desired vector field can be replaced by

$$V_{new}(\xi,\eta) = \begin{cases} V(\xi,\eta) \text{ if } (\xi,\eta) \in \text{important points}, \\ (0,0), \text{ otherwise.} \end{cases}$$

For instance, the "important points" can be defined as points characterized by a high curvature or large rotation angles. At the unimportant points $F_V = 0$, which simplifies the numerical solution and reduces the number of iterations. The numerical approximation is based on the discrete Laplacian and the central differences for the first derivatives.

5 KINEMATIC ERROR

Let $W^D(s_p, s_{p+1}, t) \in S(u,v)$ be a desired trajectory between two tool positions W_p and W_{p+1}, where $t \in [s_p, s_{p+1}]$ is a parametric coordinate along the curve. The kinematic error is a distance between $W^D(s_p, s_{p+1}, t)$, and the actual trajectories $W(s_p, s_{p+1}, t)$ are defined as follows:

$$\varepsilon = \sum_p \text{dist}(W^D(s_p, s_{p+1}, t), W(s_p, s_{p+1}, t)). \quad (5)$$

The actual trajectories are generated by the inverse kinematic transformations (see, for instance, [47], pages 40-42). Furthermore, we use a parameterization-invariant Hausdorff distance, given by

$\text{dist}_H(W, W^D) = \max\{\max_{a \in W(t)} \min_{b \in W^D(t)} |a-b|_E, \max_{b \in W^D(t)} \min_{a \in W(t)} |a-b|_E\}$, where the subscript E denotes the Euclidean distance.

6. BIASED SPACE FILLING CURVE

First, the curvilinear grid $\{u_{i,j}, v_{i,j}\}$ is converted into a continuous mapping $\{u(\xi,\eta), v(\xi,\eta)\}$ using the bilinear interpolation. Next, the discrete grid is reconstructed using the condition $\mathrm{dist}_H(T_i, T_{i+1}) < w_{R,i} + w_{L,i+1}$, where T_i T_{i+1} are the adjacent tool tracks, and $w_{L,i}, w_{R,i+1}$ are the left and the right maximum allowed strip width (Figure 8 (a)).

The cells are connected by the biased adaptive space filling curve (BSFC) [16] so that the toolpath follows the optimal direction, where necessary. The BSFC uses the concept of important and non-important points as a compromise between reducing the machining time and the kinematic error. The idea is similar to that used for minimization of the alignment functional. If the grid is well aligned with the optimal direction, then the BSFC follows it. However, the BSFC works on the chaotic vector fields as well. If the grid is not well aligned with the important point, the BSFC defines a local optimal direction based on an estimate of the cost function around this particular point. If the point is unimportant, the BSFC connects it with a random neighboring point. Furthermore, the algorithm detects segments characterized by the multiple consecutive turns. The BSFC along this segment is re-adjusted to follow the main direction in a window around the segment as shown in Figures 8 (b) and (c).

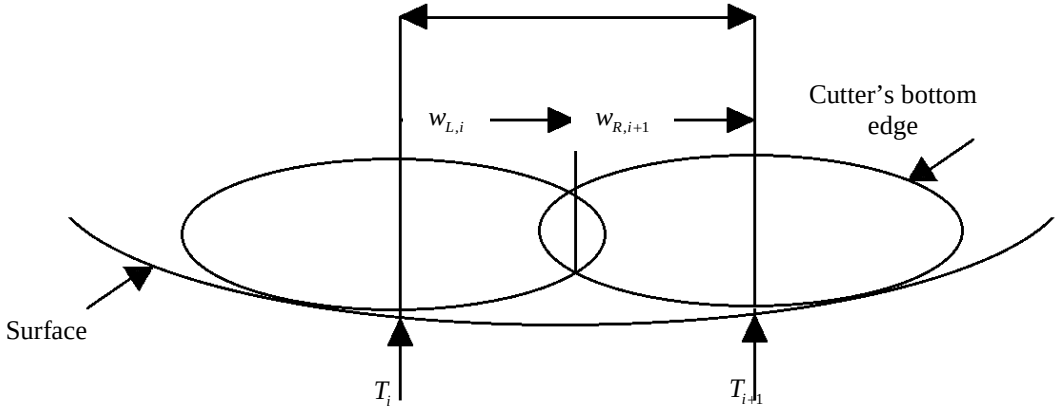

(a) Calculating the offset between the tool tracks

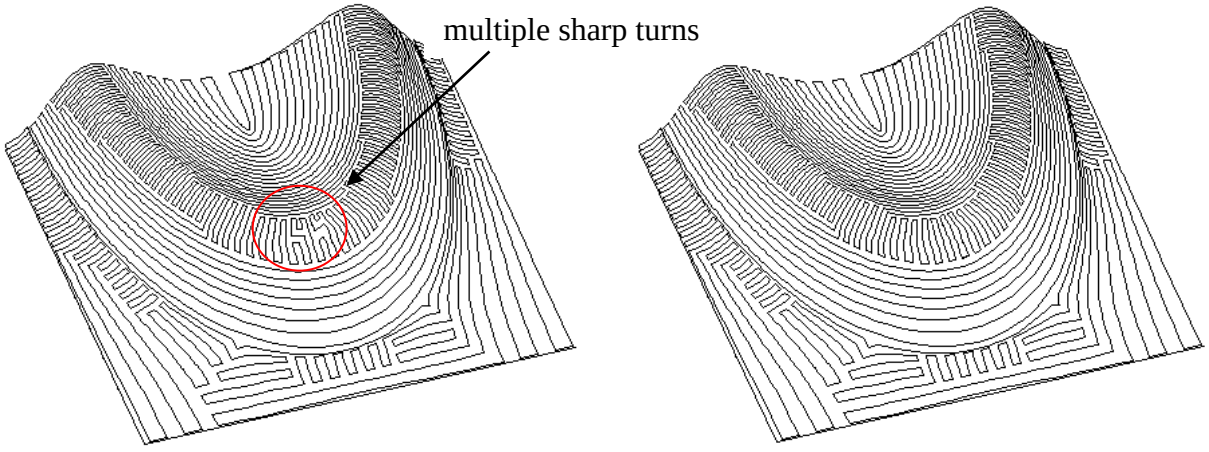

(b) Before correction (c) After correction

Figure 8. BSFC correction in the case of frequent turns

7. NUMERICAL EXAMPLES AND CUTTING EXPERIMENTS

In this section, the ACT is applied to STL toolpath generation. The numerical technology has been tested against the standard ISO, MasterCam, advanced toolpath algorithms Helical/Spiral (HS), and Follow Periphery (FP) of NX9 (formerly UG). All surfaces have been machined using a flat end cutter. The experiments have been performed for 5 axis machines MAHO-600E and HAAS VF2TR.

The conventional methods and the ACT have been applied with an appropriate setup optimization [4]. The accuracy of the machining has been evaluated in terms of the kinematic error, roughness, and waviness. The improvement is defined as $\frac{before - after}{before}100$. The grid alignment is based on cost functions representing the material removal rate and the toolpath length. We will denote these options by subscripts R and L, respectively, for instance, $VFAG_R$ and $VFAG_L$.

Example 1. Surface decomposition and ACT for a synthetic dental surface

The surface in Figure 9 (a) is characterized by a ridge nearby the boundary. We adopted this shape from the dental milling, where the elevated part represents the ridges of a dental crown or implant [48]. The size of the workpiece is 100x100. The surface was designed using MasterCam, then converted into the STL format (Figure 9 (a)), and flattened using the proposed radial plane approach (Figure 9 (b)).

The VFAG for such surfaces can be efficiently generated in subregions obtained automatically or manually. Clearly, the surface is composed of a flat region and a region characterized by a high curvature. The high curvature narrows the machining strip, whereas inside the flat area, the tool can cut the material using the maximum machining strip. The optimal directions corresponding to the material removal rate and machining strip width, respectively, in Figures 9 (c) and (d), show that it is possible to construct a single grid such that one family of the grid lines is adapted to V_R and another to V_L.

Consider the case when the user requires a minimal tool path for the rough cut to reduce the tool wear and the minimal time for the fine cut. The generated VFAG in Figure 9 (e) accomplishes both tasks. The rough machining is performed along the direction of the highest curvature, in order to maximize the machining strip (ACT_L). The finishing strategy employs ACT_R to maximize the material removal rate and to reduce the machining time. In this case, most of the time the tool moves along the direction of the minimal curvature. Note that a boundary fitted grid in Figure 9 (f) was used as the initial approximation for VFAGs. The toolpaths, constructed by BSFC, are shown in Figures 9 (g) and (h). Clearly, the two cost functions generate very different toolpaths. The virtual and real machining results are illustrated in Figures 9 (i)-(l).

The performance of ACT, in terms of the length of the toolpath and the machining time, is summarized in Table 1. The table clearly demonstrates the advantages of the ACT_L and ACT_R for varying scallop height. The benchmark methods are the regular ISO, MasterCam, and advanced algorithms, HS and FP of NX9.
Compared to ISO, the length of the ACT_L-path is shorter by 7-20%. For instance, when the maximum allowable scallop height h=0.01, the length of the tool path is about 2,500 mm shorter while the entire ISO is approximately 12000mm. The machining time for the fine cut

using ACT_R has been reduced by 76%. In other words, the proposed method reduces the machining time by (approximately) a factor of 2. There is a clear advantage relative to NX9. For instance, on MAHO 600E for h=0.01, the ACT_R requires 19 min versus 46 min using FP, and 9h52min using HS (see the entire evaluation in Table 1).

Table 2 compares the quality of the proposed method vs. ISO in terms of the average kinematic error $\bar{\varepsilon}$, the corresponding standard deviation σ_ε and the number of the required CC points N_{CC}. Clearly, the error stays within the prescribed limits, whereas the number of the CC points has been reduced. For instance, for HAAS VF-2TR $N_{CC,ISO}=18603$, $N_{CC,R}=9625$, and $N_{CC,L}=17437$.

Table 3 shows the quality of the produced surface for the rough and finishing cuts evaluated by stylus profiling, [49]. The surface profile obtained by a high-resolution probe is post processed by the Gaussian filter [50]. Twenty sample profiles were measured with the standard cutoff of 0.8 mm [50]. Roughness of the machined surface is within the acceptable range for surface milling operations [51]. The rough cut by the ACT_L has a better quality compared to ISO, that is, roughness: 7.8 vs. 8.1 μm and waviness 17.8 vs. 31.9. We hypothesize that the major improvement in waviness is due to a reduced variation of the rotation angles, which are implicitly included in the evaluation of the material removal rate, since maximization of the removal rate leads to the reduction in the angular distance between the CC points.

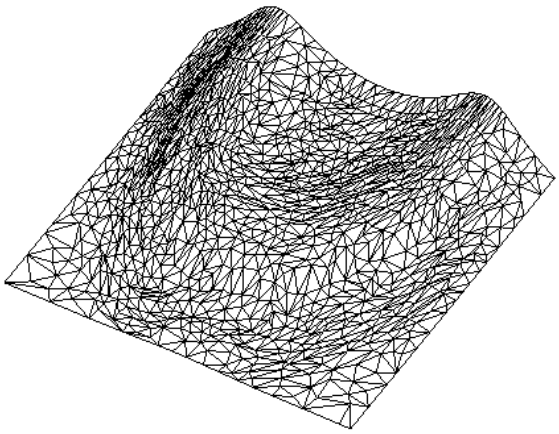

(a) Synthetic dental surface

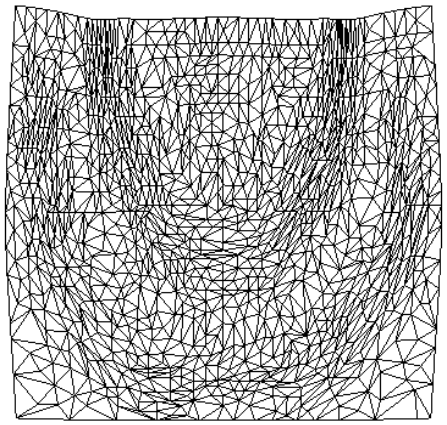

(b) Flattened surface

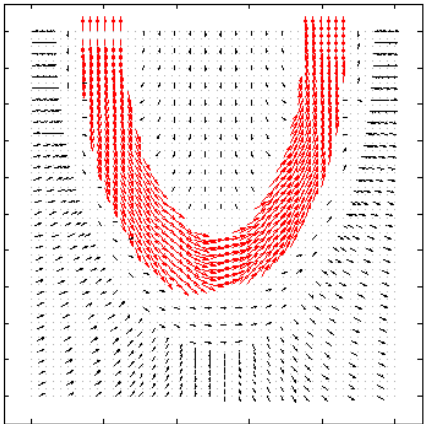

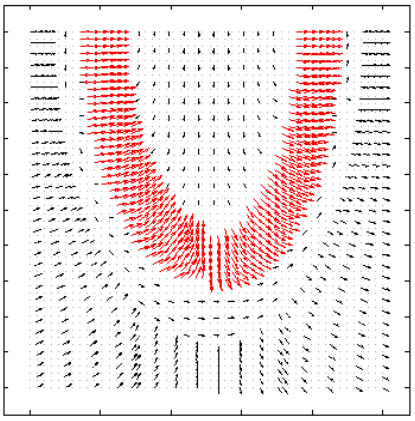

(c) V_R

(d) Vector field V_L

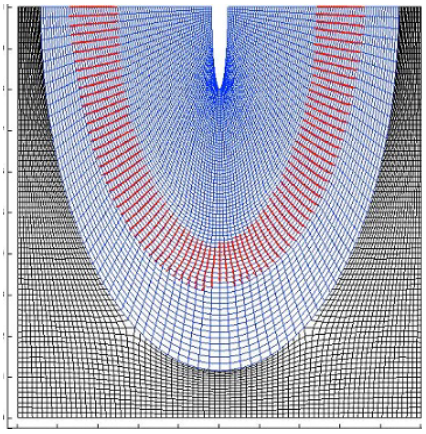

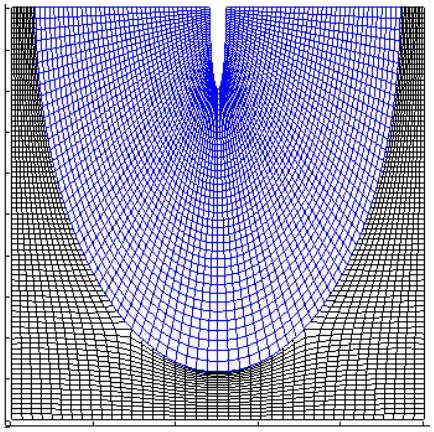

(e) VFAG

(f) Boundary fitted grid

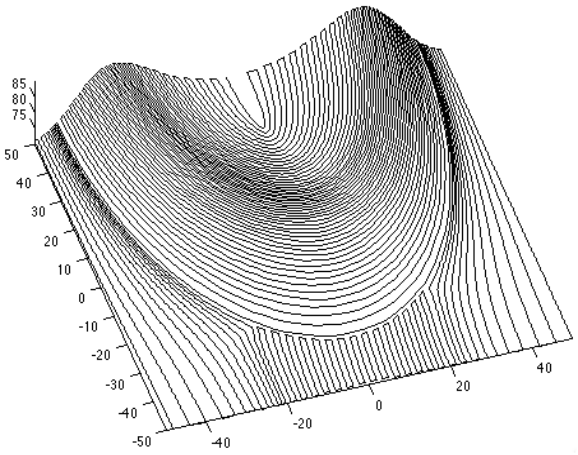

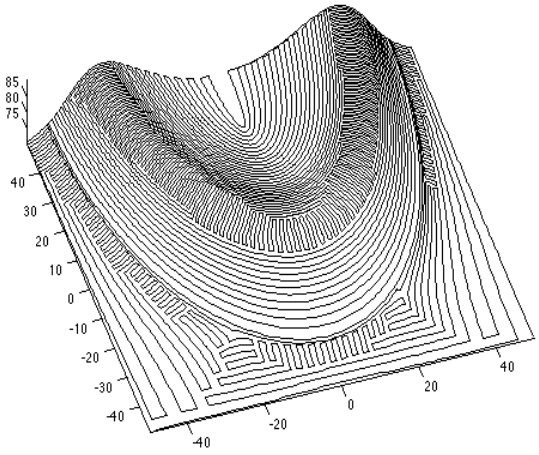

(g) ACT_R

(h) ACT_L

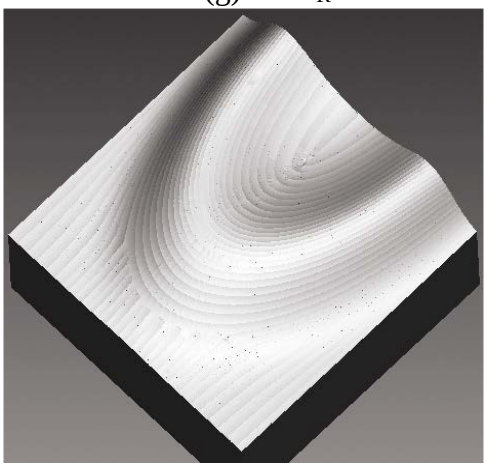

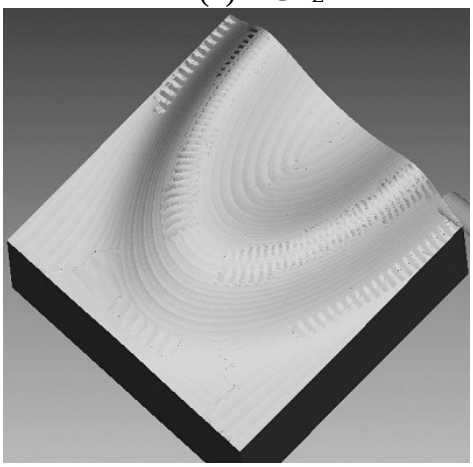

(i) Virtual ACT_R

(j) Virtual ACT_L

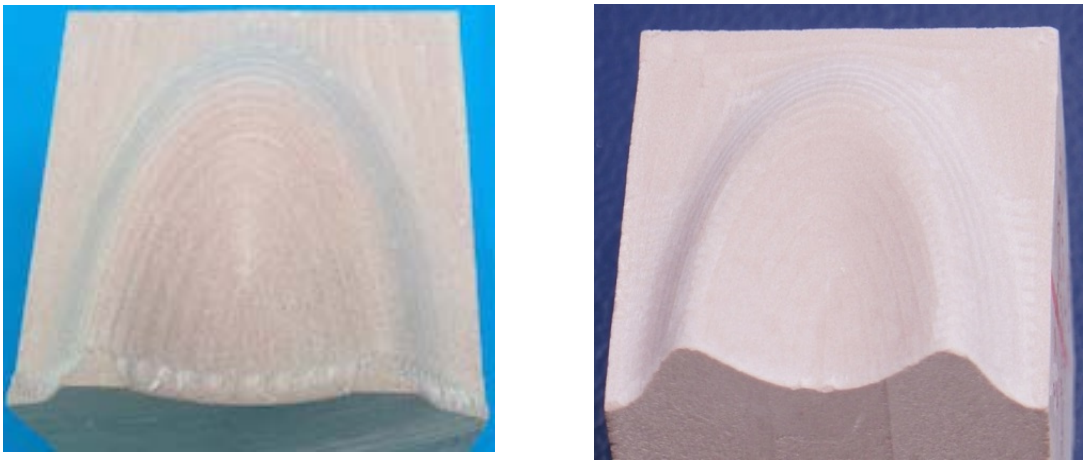

(k) Machining by ACT_R (l) Machining by ACT_L

Figure 9. Synthetic (ridge-cusp) dental surface

Table 1 Synthetic dental surface: ACT vs. the reference methods

	Toolpath Generation Methods			Scallop Height h (mm)		
				0.25	**0.10**	**0.05**
Performance	**Toolpath Length (mm)**		**Master CAM**	35553.0	72215.0	128879.0
			HS	25991.0	62825.0	125070.0
			FP	5480.4	8115.6	11175.0
			ISO	5755.2	8666.1	12034.0
			ACT_R	5489.1	7601.2	10075.0
			ACT_L	5336.9	7092.7	9545.7
	Machining Time	**HAAS VF2TR**	**HS**	3:26:00.6	8:13:54.1	16:22:50.4
			FP	0:45:04.7	1:07:20.4	1:33:35.8
			ISO	0:56:13.9	1:26:37.5	2:01:03.5
			ACT_R	0:17:46.1	0:24:56.1	0:33:36.1
			ACT_L	0:55:09.7	1:24:21.2	1:55:52.1
		MAHO 600E	**HS**	2:03:53.1	4:57:21.7	9:52:27.2
			FP	0:22:15.4	0:33:09.6	0:46:22.0
			ISO	0:28:22.1	0:43:39.8	1:01:03.8
			ACT_R	0:10:25.4	0:14:21.7	0:19:22.9
			ACT_L	0:27:14.5	0:41:20.4	0:56:19.7
Advantage rel. to ISO	**Toolpath Length (mm)**		**ACT_R**	4.6%	12.3%	16.3%
			ACT_L	7.3%	18.2%	**20.7%**
	Machining Time	**HAAS VF2TR**	**ACT_R**	68.4%	71.2%	**72.2%**
			ACT_L	1.9%	2.6%	4.3%
		MAHO 600E	**ACT_R**	63.3%	67.1%	**68.3%**
			ACT_L	4.0%	5.3%	7.8%

Table 2 Synthetic dental surface: CC points, kinematic error, ACT vs. ISO

Toolpath Generation techniques	HAAS VF-2TR									MAHO 600-E								
	h=0.25 mm			h=0.10 mm			h=0.05 mm			h=0.25 mm			h=0.10 mm			h=0.05 mm		
	N_{CC}	$\bar{\varepsilon}$	σ_ε	N_{CC}	$\bar{\varepsilon}$	σ_ε	N_{CC}	$\bar{\varepsilon}$	σ_ε	N_{CC}	$\bar{\varepsilon}$	σ_ε	N_{CC}	$\bar{\varepsilon}$	σ_ε	N_{CC}	$\bar{\varepsilon}$	σ_ε
ISO	5882	0.082	0.064	10299	0.040	0.024	18603	0.023	0.012	5047	0.064	0.063	9334	0.038	0.025	16652	0.022	0.012
ACT_R	5378	0.013	0.010	7157	0.013	0.008	9625	0.011	0.004	5374	0.009	0.004	7151	0.009	0.001	9331	0.009	0.001
ACT_L	4321	0.065	0.006	9418	0.025	0.026	17437	0.013	0.013	4059	0.054	0.002	9059	0.022	0.025	16773	0.012	0.013

Table 3 Synthetic dental surface: roughness and waviness, ACT vs. ISO

Roughness R_a (μm)			Standard Deviation			Waviness R_a			Standard Deviation		
ISO	**ACT_R**	**ACT_L**	**ISO**	**ACT_R**	**ACT_L**	**ISO**	**ACT_R**	**ACT_L**	**ISO**	**ACT_R**	**ACT_L**
8.1	6.8	7.8	10.5	3.1	8.1	31.9	12.2	17.8	7.5	1.5	6.2

Example 2. Dual vector field on a single Cartesian grid. STL model of the human face mask.

The ACT applied to the surface from Example 1 employs decomposition techniques to achieve the best alignment with the vector field. However, certain surfaces allow for a decomposition of the vector field $V(u,v)$ into a dual vector field $V_D(u,v) = (\alpha(u,v), \beta(u,v))$ and adaptation of the two families of the coordinate curves to $\alpha(u,v)$ and $\beta(u,v)$, respectively, within a single parametric region (see Section 4).

We apply these techniques to an STL model of the human face mask in Figure 10 (a), (b). The two families of vector fields shown in Figures 10 (c) and (d) are obtained using V_R while Figure 10 (e) and (f) show the vector field obtained using V_L. The VFAGs are presented in Figures 10 (g) and (h). The particular cost function affects BSFCs displayed in Figures 10 (i) and (j). Virtual and real machining using the regular ISO and ACT_R are presented in Figures 10 (k) - (m) and Figures 10 (l) - (n), respectively.

Table 4 presenting the performance of the ACT against the benchmark toolpath generation methods shows the advantages of the proposed framework. The ACT_L is shorter by 17% and the ATC_R is faster by 13%, compared to ISO. Note that the real industrial parts require thousands of hours of costly machine operations and qualified technicians. Therefore, the advantage of 13-17% is financially and technically sound. Besides, the example shows that even for a very complicated surface and seemingly chaotic vector field, the ACT based on a single VFAG can lead to important improvements (our next example shows that those improvements can be even more tangible). Table 5 shows that the efficiency of the ACT measured by the number of the required CC increases, whereas the average kinematic error practically does not change. Finally,

Table **6** displaying the roughness and waviness of the machined surface measured by stylus profiling, shows the advantages of the ACT.

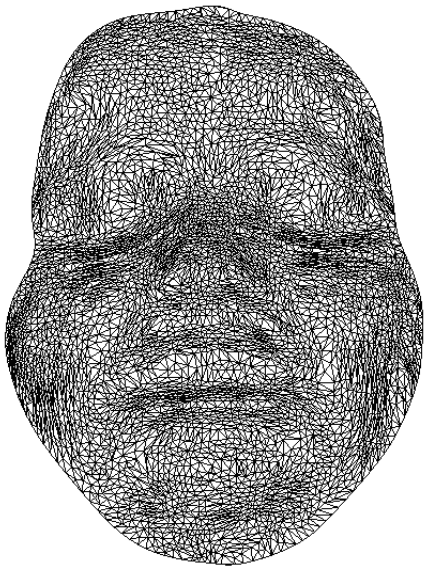

(a) Human mask

(b) Flattened human mask

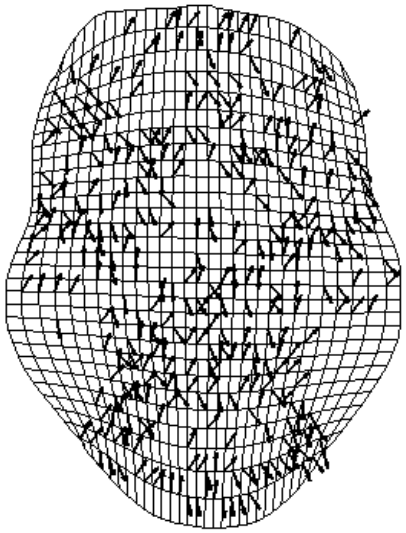

(c) $\alpha_R(u,v)$

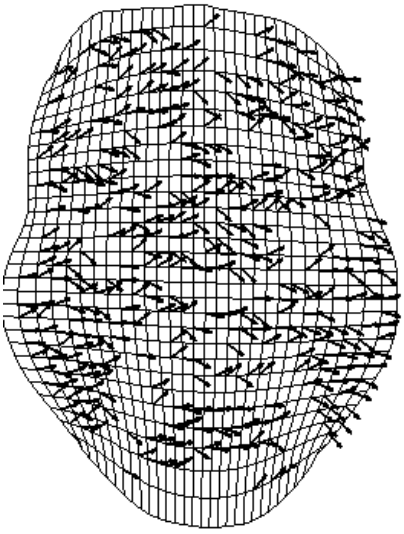

(d) $\beta_R(u,v)$

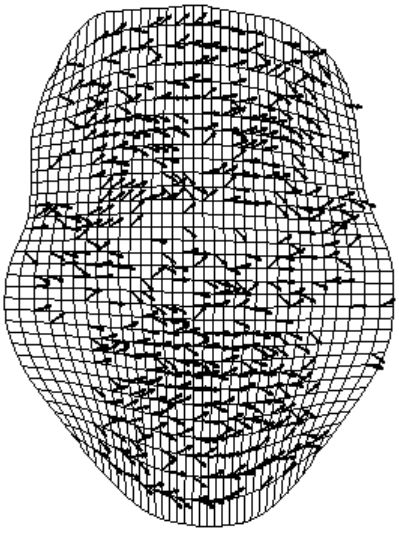

(e) $\alpha_L(u,v)$

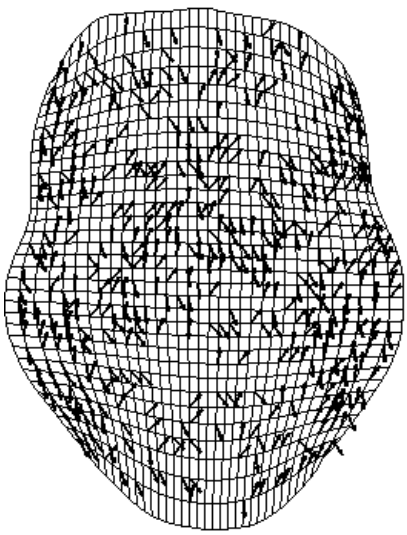

(f) $\beta_L(u,v)$

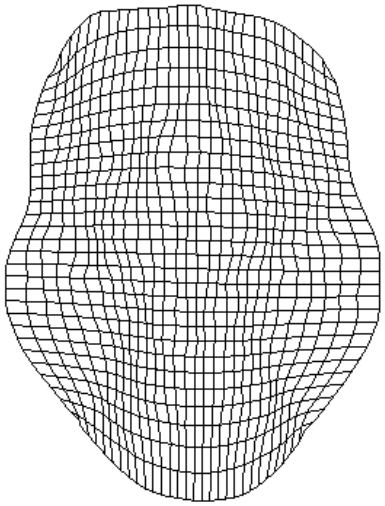

(g) $VFAG_R$

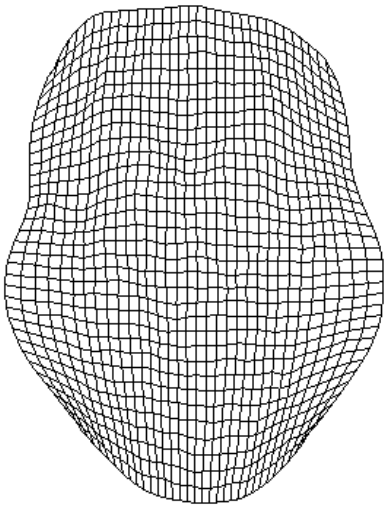

(h) $VFAG_L$

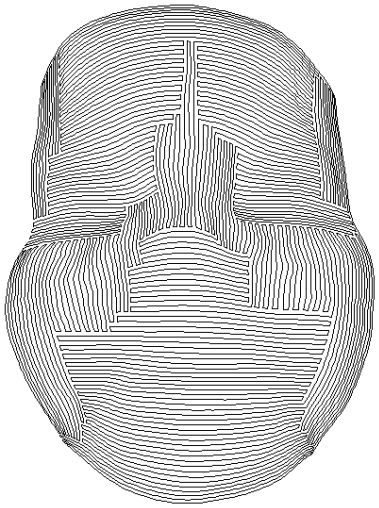

(i) $BSFC_R$

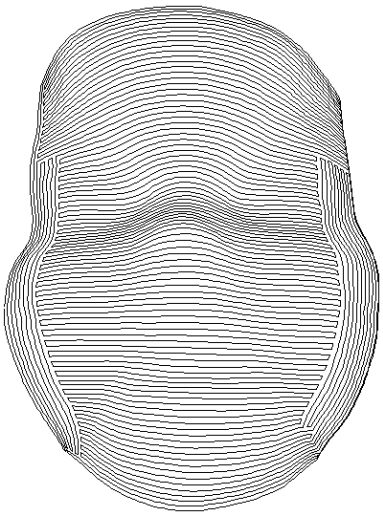

(j) $BSFC_L$

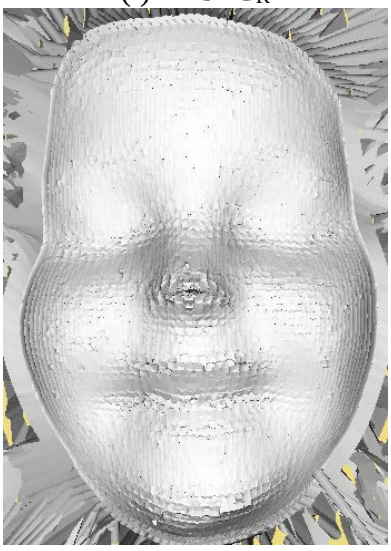

(k) Virtual machining, ISO

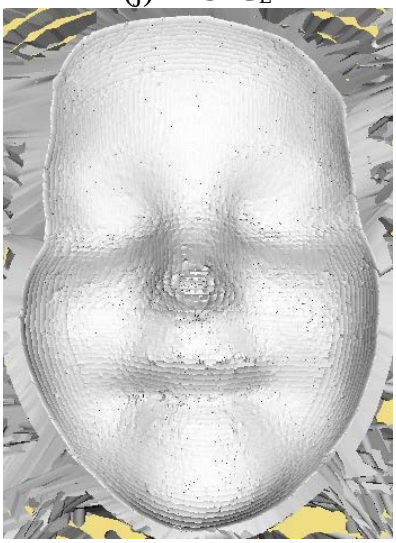

(l) Virtual machining, ACT_R

(m) Real machining, ISO

(n) Real machining, ACT_R

Figure 10. Machining the human face mask

Table 4 Human face surface: ACT vs. the reference methods

	Toolpath Generation Methods			Scallop Height (mm)		
				0.25	**0.10**	**0.05**
Performance	**Toolpath Length (mm)**		**Master CAM**	17372.6	37669.5	71054.5
			HS	2968.6	7072.1	13988.8
			FP	3224.6	3241.2	4426.2
			ISO	3115.6	3203.0	4072.0
			ACT_R	2944.9	2961.8	3530.1
			ACT_L	2681.3	2671.1	3364.0
	Machining Time	**HAAS VF2TR**	**HS**	0:24:42.0	0:57:53.8	1:53:36.8
			FP	0:48:24.1	0:48:48.2	1:07:05.6
			ISO	0:54:27.4	0:55:59.7	1:11:29.1
			ACT_R	0:51:57.2	0:51:43.1	1:02:10.3
			ACT_L	0:53:30.3	0:54:41.2	1:09:30.9
		MAHO 600E	**HS**	0:18:18.6	0:42:44.2	1:23:53.4
			FP	0:24:57.8	0:25:17.8	0:34:30.2
			ISO	0:17:52.6	0:18:24.9	0:23:27.5
			ACT_R	0:17:11.1	0:17:04.4	0:20:50.5
			ACT_L	0:17:39.2	0:18:07.3	0:22:57.1
Advantage rel. to ISO	**Toolpath Length (mm)**		**ACT_R**	5.5%	7.5%	13.3%
			ACT_L	13.9%	16.6%	**17.4%**
	Machining Time	**HAAS VF2TR**	**ACT_R**	4.6%	7.6%	**13.0%**
			ACT_L	1.7%	2.3%	2.8%
		MAHO 600E	**ACT_R**	3.9%	7.3%	11.2%
			ACT_L	1.2%	1.6%	2.2%

Table 5 Human face surface: CC points, kinematic error, ACT vs. ISO

Toolpath Generation techniques	HAAS VF-2TR									MAHO 600-E								
	h=0.25 mm			h=0.10 mm			h=0.05 mm			h=0.25 mm			h=0.10 mm			h=0.05 mm		
	N_{CC}	$\overline{\varepsilon}$	σ_ε	N_{CC}	$\overline{\varepsilon}$	σ_ε	N_{CC}	$\overline{\varepsilon}$	σ_ε	N_{CC}	$\overline{\varepsilon}$	σ_ε	N_{CC}	$\overline{\varepsilon}$	σ_ε	N_{CC}	$\overline{\varepsilon}$	σ_ε
ISO	1509	0.081	0.616	3936	0.056	0.183	6917	0.050	0.031	1260	0.050	0.154	1221	0.028	0.064	3132	0.022	0.060
ACT_R	1446	0.060	0.179	3896	0.035	0.104	6832	0.028	0.018	1171	0.034	0.076	1206	0.019	0.049	2704	0.009	0.030
ACT_L	1023	0.061	0.077	2822	0.035	0.036	4911	0.025	0.029	275	0.026	0.050	962	0.018	0.027	1941	0.013	0.020

Table 6 Human face surface, roughness and waviness, ACT vs. ISO

Roughness R_a (μm)		Standard Deviation		Waviness R_a		Standard Deviation	
ISO	**ACT_R**	**ISO**	**ACT_R**	**ISO**	**ACT_R**	**ISO**	**ACT_R**
8.3	8.1	7.7	7.7	43.6	40.8	23.8	28.6

Example 3. Dual vector field on a single Cartesian grid. An STL model of the incisor tooth.

We verify our methodology on the STL models of four types of human teeth: incisor, premolar, molar, and canine. The STL model of the incisor and the corresponding flattened STL are presented in Figure 11. The incisor represents the case when the dual vector field on a single Cartesian grid leads to the significant improvement, in terms of the length of the tool path and the machining time. The components of the dual vector fields $V_{D,R}(u,v) = (\alpha_R(u,v), \beta_R(u,v))$ and $V_{D,L}(u,v) = (\alpha_L(u,v), \beta_L(u,v))_L$ are shown on the surface and in the parametric domain in Figures 11 (c) - (h). VFAGs are presented in Figures 11 (i) - (l). Finally, machined surfaces are shown in Figures 11 (m) - (n). Table 7 shows the benefits. The toolpath is 43% shorter and 46% faster against the standard ISO. The advantage with regard to NX9, in terms of the length of the tool path, is also very significant. For instance, when h=0.01, the ACT_L generates the tool path of 570.9 whereas the best NX9 result is 1049.3. The advantage in the machining time on HAAS is 17%. It should be noted that the neither MasterCam nor NX9 can produce the 5 axis tool path for the STL surface directly**.** In order to compare their performance, we flattened the STL surface, generated a boundary fitted curvilinear grid, and approximated the surface on that grid. Therefore, our MasterCam and NX9 toolpath generation is partly based on the proposed techniques. Finally, Table 9 shows that the efficiency of the ACT, measured by the number of the required CC points, increases, whereas the average kinematic error practically does not change.

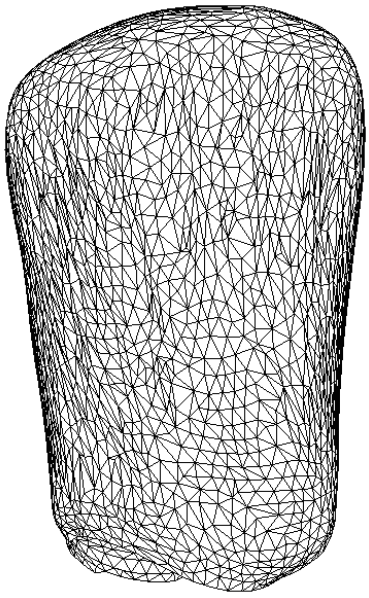

(a) STL model of the incisor

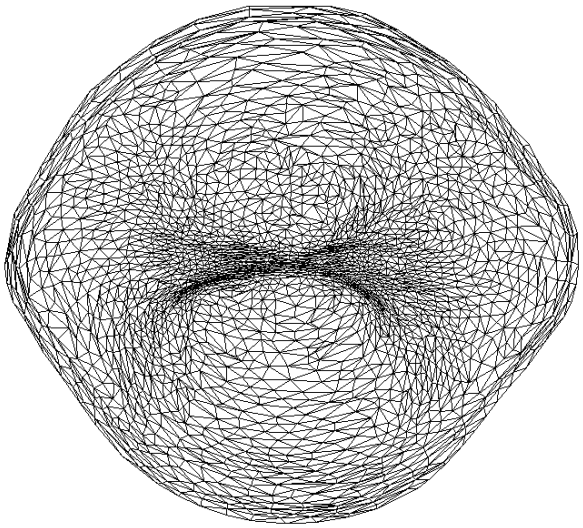

(b) flattened incisor

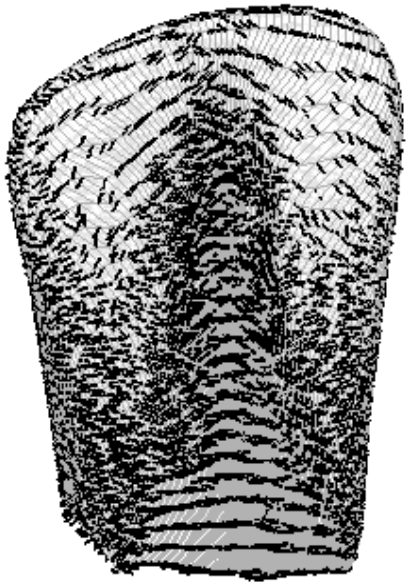

(c) V_R

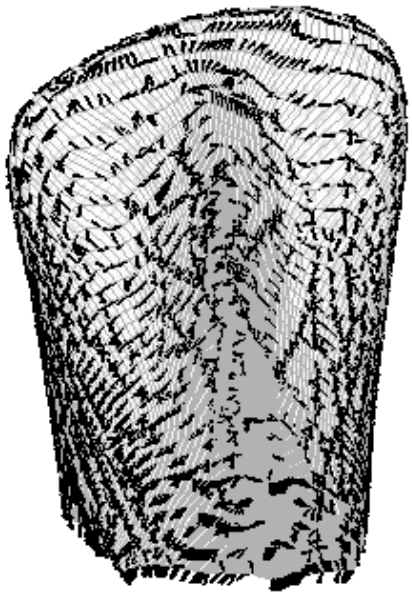

(d) V_L

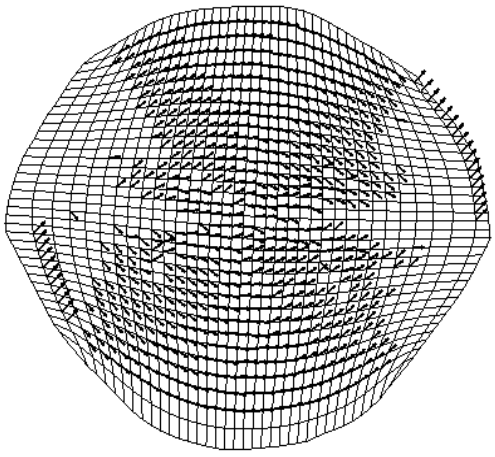

(e) $\alpha_R(u,v)$

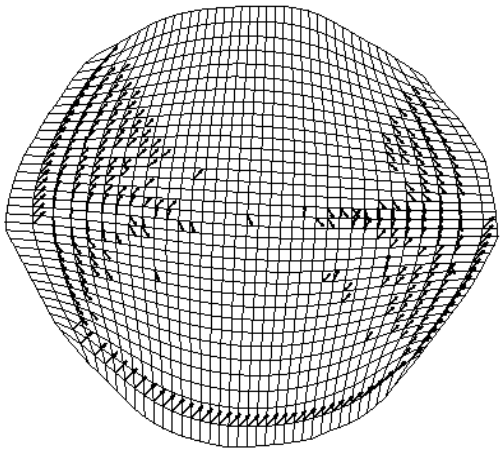

(f) $\beta_R(u,v)$

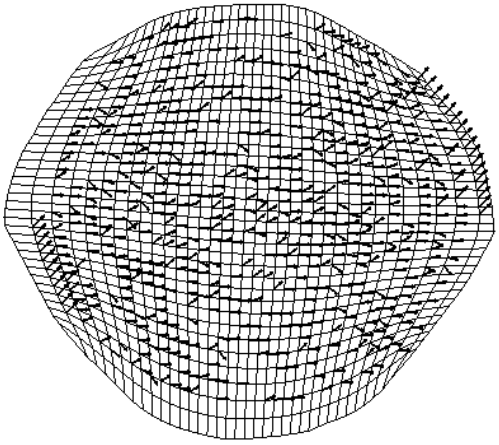

(g) $\alpha_L(u,v)$

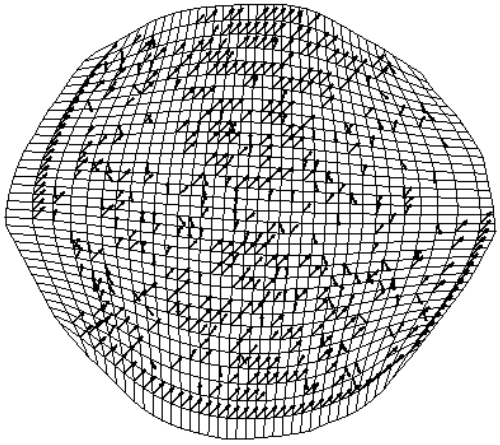

(h) $\beta_L(u,v)$

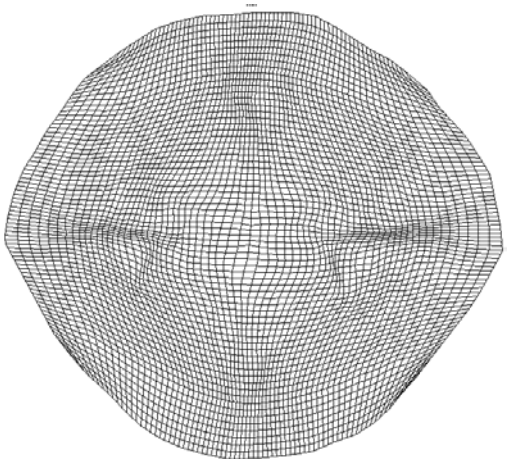

(i) $VFAG_R$

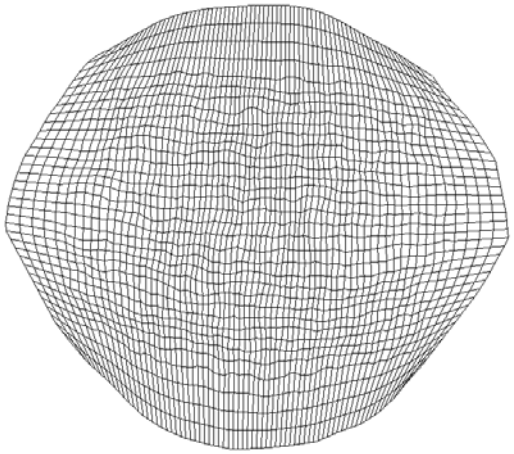

(j) $VFAG_L$

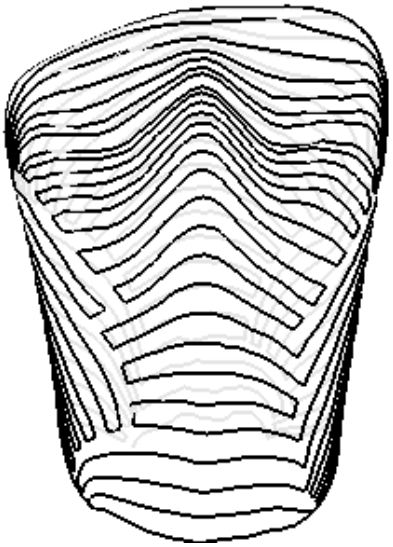

(k) $BSFC_R$

(l) $BSFC_L$

(m)Virtual milling, ACT_R

(n) Virtual milling, ACT_L

Figure 11. Machining the incisor tooth

Table 7 Incisor tooth: ACT vs. the reference methods

	Toolpath Generation Methods			Scallop Height (mm)		
				0.065	**0.025**	**0.0125**
Performance	**Toolpath Length (mm)**		**Master CAM**	6834.8	14373.3	27614.1
			HS	655.9	1477.7	2781.5
			FP	800.1	940.4	1049.3
			ISO	756.4	837.9	1005.5
			ACT R	469.1	515.6	582.9
			ACT L	456.0	498.5	570.9
	Machining Time	**HAAS VF2TR**	**HS**	0:18:22.0	0:40:40.2	1:19:15.1
			FP	0:21:13.4	0:28:27.7	0:30:50.6
			ISO	0:34:19.2	0:38:35.2	0:46:14.4
			ACT R	0:19:47.5	0:21:34.2	0:25:02.3
			ACT L	0:24:50.6	0:27:11.2	0:31:25.2
		MAHO 600E	**HS**	0:07:34.5	0:16:48.4	0:32:04.6
			FP	0:07:30.5	0:08:53.7	0:09:55.8
			ISO	0:11:10.7	0:12:49.0	0:15:38.9
			ACT R	0:07:13.9	0:07:56.6	0:09:11.0
			ACT L	0:07:13.1	0:08:09.3	0:09:33.1
Advantage ref. to ISO	**Toolpath Length (mm)**		**ACT R**	38.00%	38.5%	42.0%
			ACT L	39.70%	40.5%	43.2%
	Machining Time	**HAAS VF2TR**	**ACT R**	42.30%	44.1%	45.9%
			ACT L	27.60%	29.5%	32.0%
		MAHO 600E	**ACT R**	35.30%	38.0%	41.3%
			ACT L	35.40%	36.4%	39.0%

Table 8 Incisor tooth : CC points, kinematic error, ACT vs. ISO

	HAAS VF-2TR									MAHO 600-E								
	h=0.065 mm			h=0.025 mm			h=0.0125 mm			h=0.065 mm			h=0.025 mm			h=0.0125 mm		
	N_{CC}	$\overline{\varepsilon}$	σ_ε	N_{CC}	$\overline{\varepsilon}$	σ_ε	N_{CC}	$\overline{\varepsilon}$	σ_ε	N_{CC}	$\overline{\varepsilon}$	σ_ε	N_{CC}	$\overline{\varepsilon}$	σ_ε	N_{CC}	$\overline{\varepsilon}$	σ_ε
ISO	576	0.048	0.173	1709	0.030	0.136	4880	0.021	0.122	36	0.013	0.029	246	0.011	0.026	1282	0.008	0.024
ACT_R	222	0.044	0.069	923	0.026	0.056	2545	0.016	0.072	7	0.010	0.023	99	0.009	0.017	611	0.006	0.013
ACT_L	574	0.051	0.178	1443	0.031	0.134	3425	0.027	0.109	60	0.014	0.032	350	0.009	0.024	1137	0.007	0.024

Example 4. C–grids applied to the STL models of canine, premolar, and molar teeth

The following three cases of the STL surfaces, corresponding to premolar, molar, and canine teeth, are characterized by the unstructured (chaotic) vector field. Consequently, VFAGs do not produce any improvement, even though the grids can be aligned with some small clusters of the vectors. However, we show that the tools provided by the ACT still can be used to improve the quality of the toolpath generation. We show that, boundary fitted curvilinear tool path, combined with a manual selection of the type of the grid and BSFC, lead to a substantial improvement.

In the context of the grid generation technologies, the basic Cartesian grids include H-grids, O-grids, and C- grids[20,52]. We will show the premolar, molar, and canine STL models can be produced using the O-grid for a shorter time, using a shorter tool path.

The STL-premolar and its flattened version are presented in Figures 12 (a) - (d). The boundary fitted initial grids in Figures 12 (e) and (f) are the H-grid and the O-grid respectively. In order to evaluate the suitability of the grid, we compute the alignment functional (3) as follows:

$F_{V,H,canine}=16.0$, $F_{V,O,canine}=14.0$, $F_{V,H,premolar}=16.7$, $F_{V,O,premolar}=14.0$, $F_{V,H,molar}=19.3$, $F_{V,O,molar}=17.6$.

Clearly, the O-grid is more suitable for the three dental models. The corresponding toolpaths and virtually machined surfaces are shown in Figures 12 (g) – (l). The results for the molar and canine teeth are displayed in Figure 13 and Figure 14. Finally, Table 9 presents the benefits of the ACT, compared to ISO and to NX9 and MasterCAM. The proposed framework provides advantages in both the toolpath length and machining time, with regard to the benchmark methods. For instance, the premolar tooth can be machined by the ACT, with the advantage of 26% in length and 43% in time relative to ISO.

Table 10 provides the number of CC points versus the scallop height and the kinematic error.

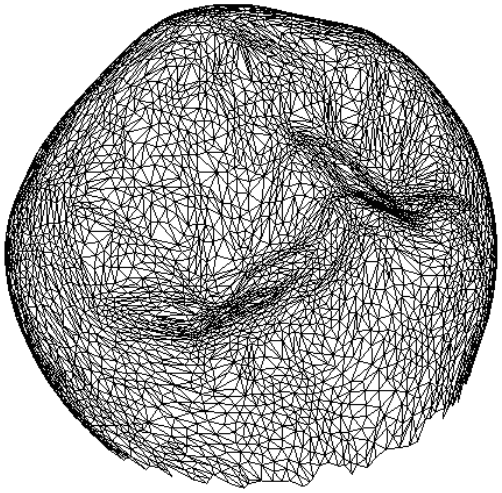

(a) STL model of the premolar tooth

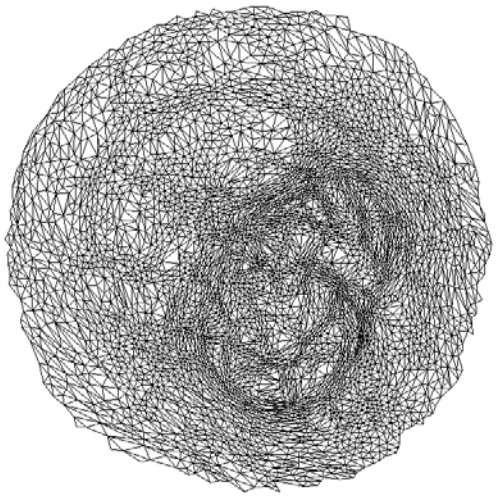

(b) flattened premolar tooth

(c) V_R

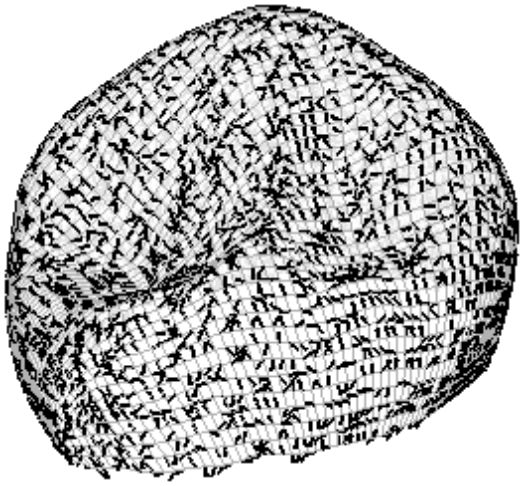

(d) V_L

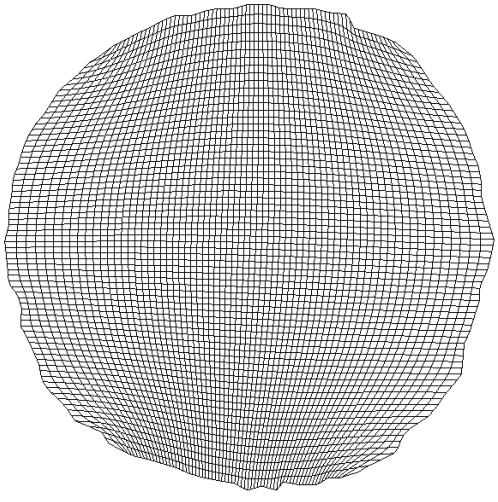

(e) H-grid

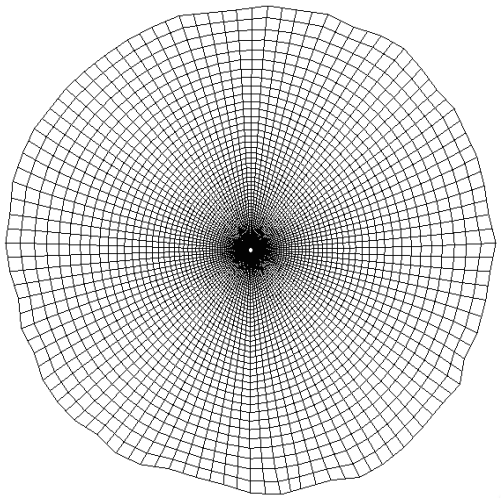

(f) O-grid

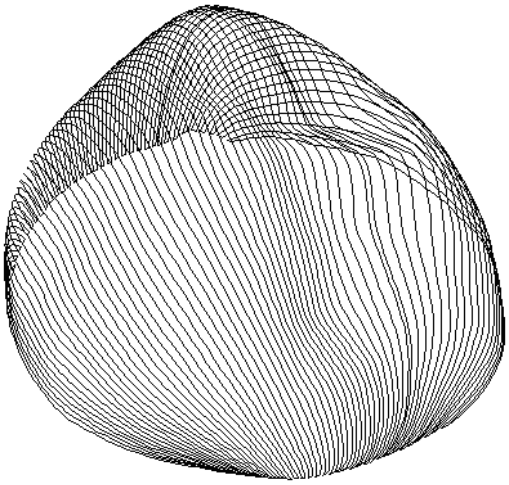

(g) ISO_H

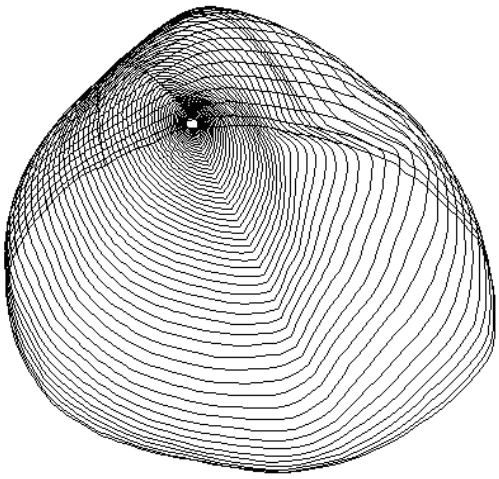

(h) ISO_O

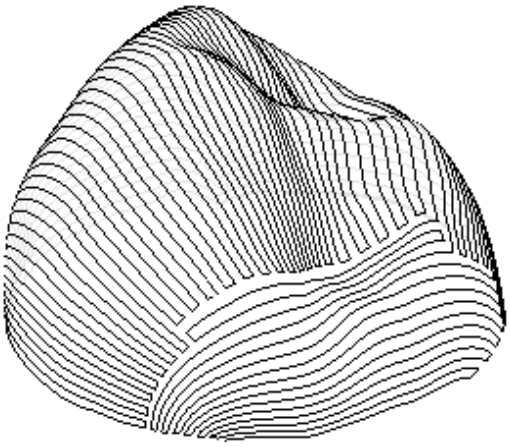

(i) $BSFC_H$

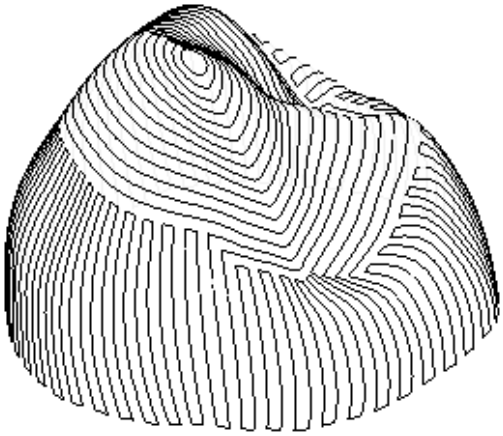

(j) $BSFC_O$

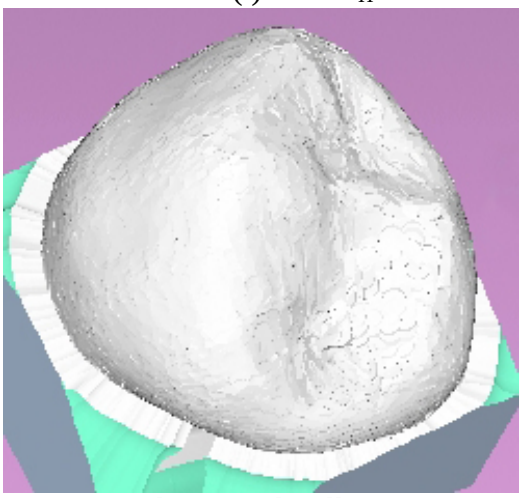

(k) Virtual milling ISO_H

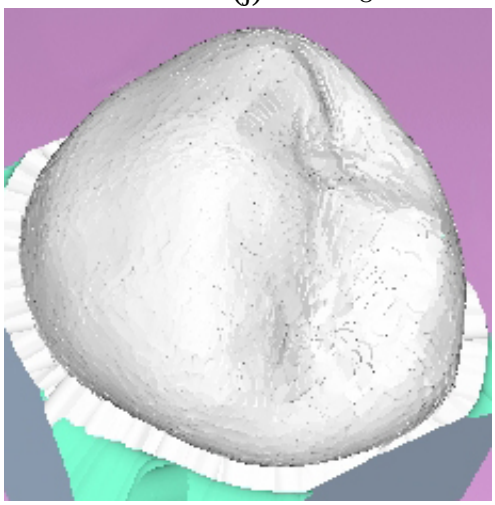

(l) Virtual milling $BSFC_O$

Figure 12. Machining the premolar tooth

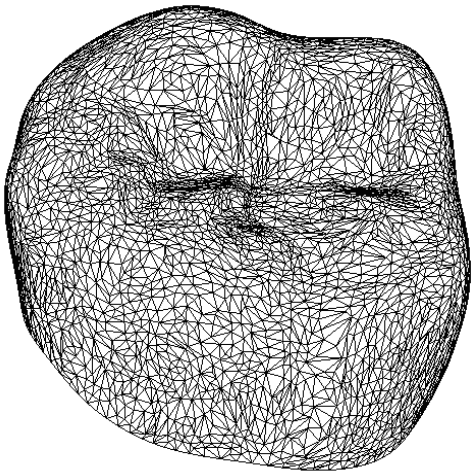

(a) STL model of the molar tooth

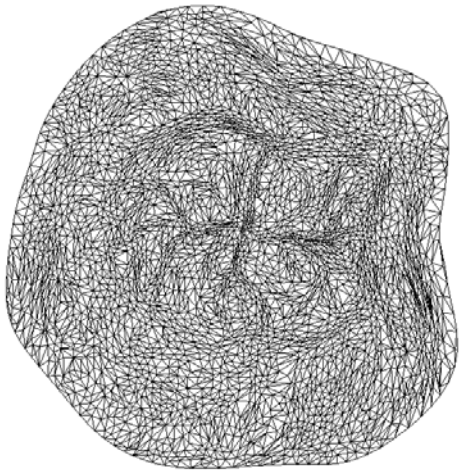

(b) flattened molar tooth

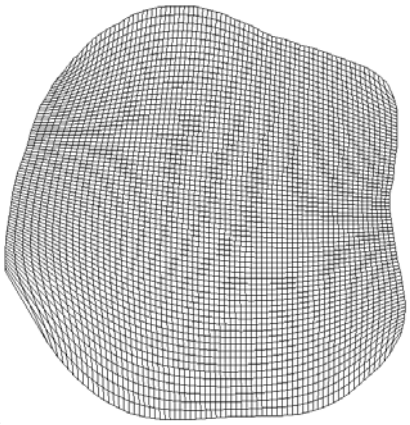

(c) H-grid

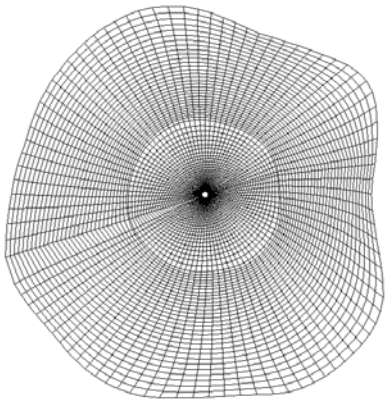

(d) O-grid

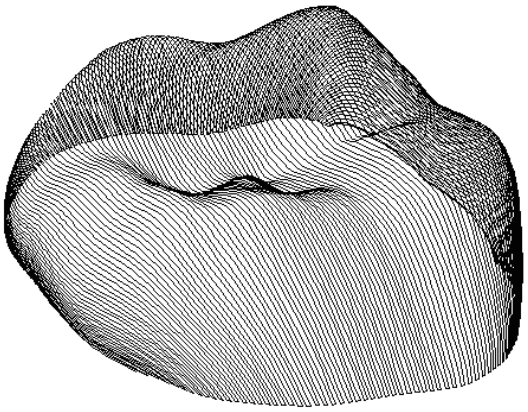

(e) ISO_H

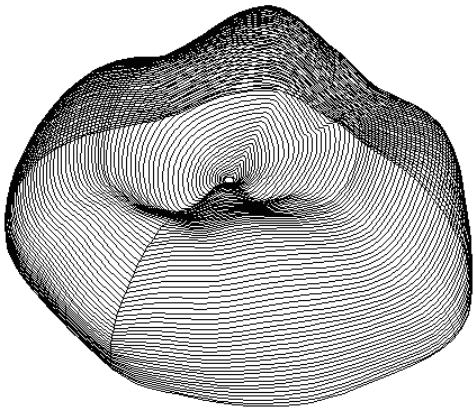

(f) ISO_O

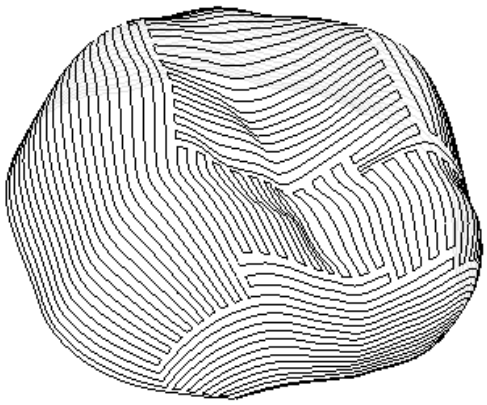

(g) $BSFC_H$

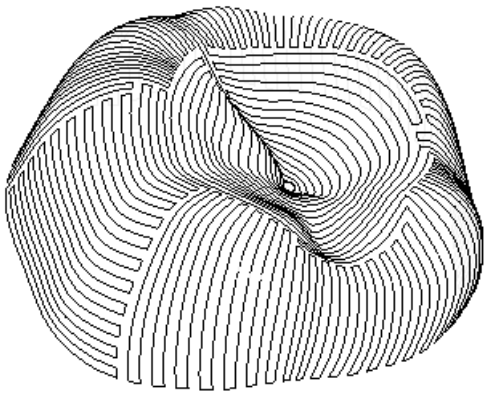

(h) $BSFC_O$

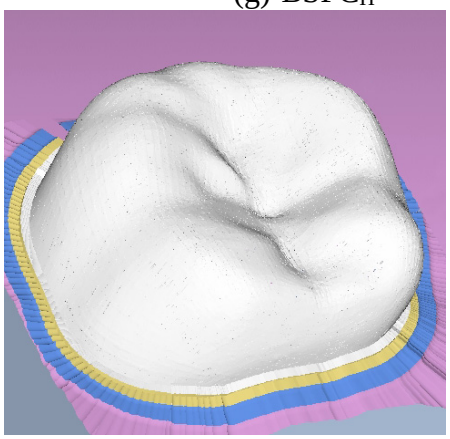

(i) Virtual milling, ISO_H

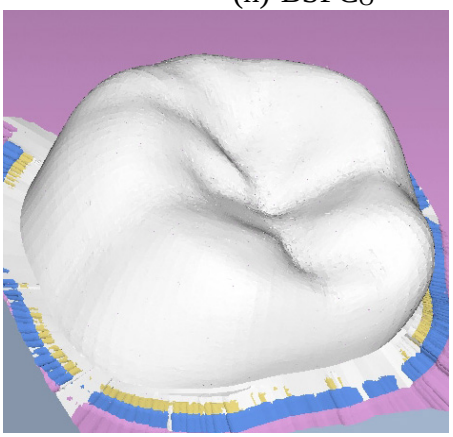

(j) Virtual milling, $BSFC_O$

Figure 13. Machining the molar tooth

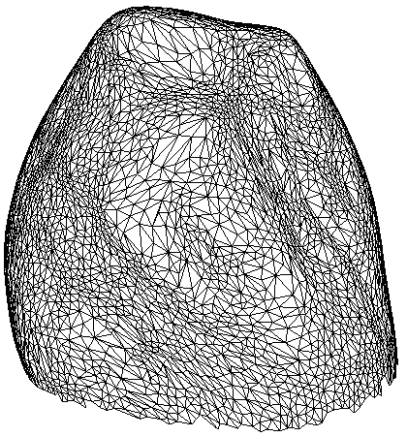

(a) STL model of a canine tooth

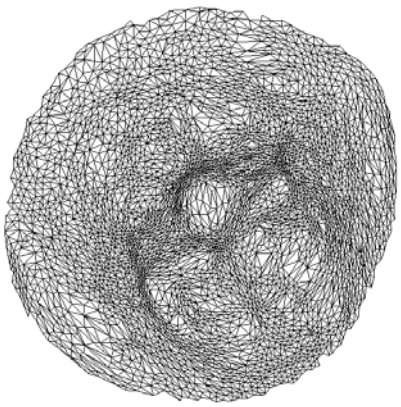

(b) Flattened canine tooth

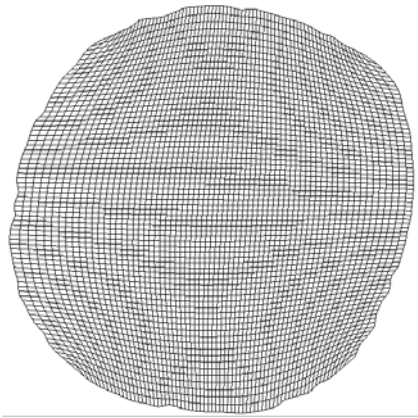

(c) H-grid

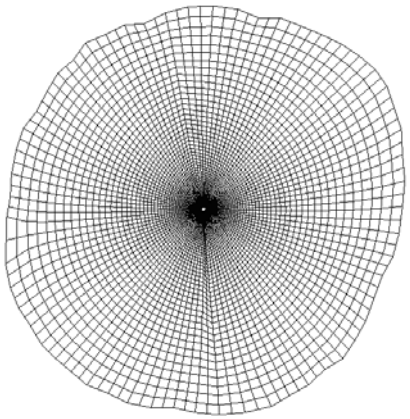

(d) O-grid

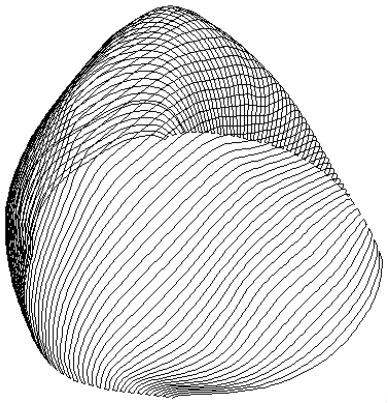

(e) ISO_H

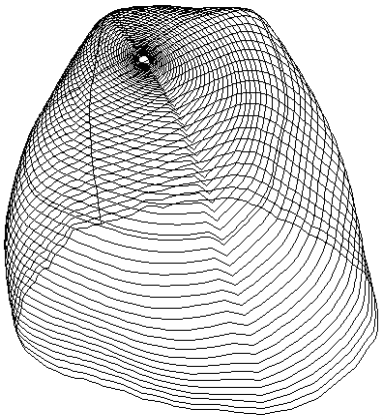

(f) ISO_O

(g) $BSFC_H$

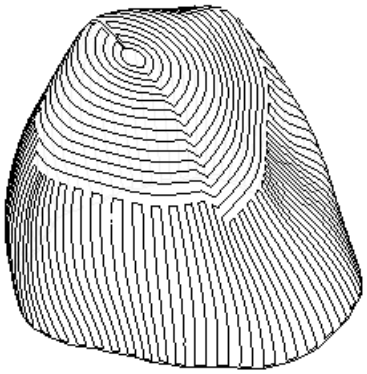

(h) $BSFC_O$

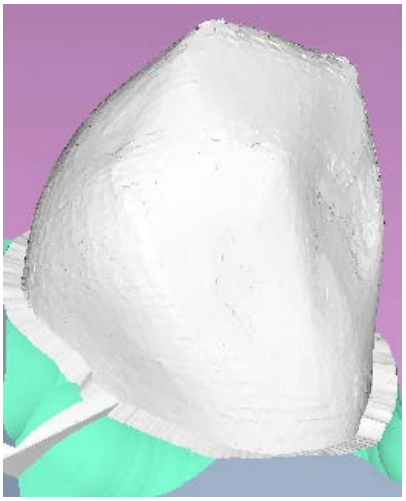

(i) Virtual Milling ISO_H

(j) Virtual Milling $BSFC_O$

Figure 14. Machining the canine tooth

Table 9 ACT vs. the reference methods, molar, premolar, and canine tooth.

	Toolpath Generation Techniques		Canine			Premolar			Molar		
			Scallop Height (mm)			Scallop Height (mm)			Scallop Height (mm)		
			0.065	0.025	0.0125	0.065	0.025	0.0125	0.065	0.025	0.0125
Performance	Toolpath Length (mm)	Master CAM	4261.3	9615.0	18802.0	5275.9	12560.3	25009.4	6483.1	15102.6	30074.0
		HS	1013.0	2330.4	4599.0	1023.5	2360.9	4614.8	1284.6	2992.0	5912.0
		FP	1120.5	1181.6	1230.2	1129.6	1156.9	1217.7	1099.9	1141.9	1184.5
		ISO	766.7	778.4	801.5	761.7	773.2	783.5	847.6	854.4	855.4
		O-Grid	664.6	664.5	664.4	616.9	622.6	620.5	826.9	827.7	828.2
		$BSFC_H$	610.7	620.3	634.3	616.1	617.5	623.5	782.5	784.8	785.4
		$BSFC_O$	617.8	627.4	641.6	573.2	574.6	580.1	742.9	745.1	745.7
	HAAS VF2TR	HS	0:20:36.5	0:47:34.7	1:33:34.8	0:24:28.4	0:56:43.5	1:50:48.3	0:37:12.3	1:27:20.7	2:51:51.9
		FP	0:24:54.2	0:26:15.4	0:27:18.8	0:34:15.9	0:35:04.8	0:36:43.3	0:37:03.1	0:38:46.2	0:39:52.8
		ISO	0:24:21.8	0:24:48.3	0:25:19.3	0:36:41.9	0:38:14.5	0:42:14.5	0:41:27.5	0:41:55.5	0:42:34.1
		O-Grid	0:22:15.8	0:22:33.5	0:22:52.9	0:28:09.1	0:28:24.6	0:30:41.5	0:35:19.5	0:35:35.1	0:35:40.0
		$BSFC_H$	0:20:55.9	0:21:05.1	0:21:07.9	0:28:44.5	0:28:50.6	0:30:30.3	0:32:47.4	0:32:55.0	0:32:58.7
		$BSFC_O$	0:20:01.9	0:20:10.7	0:20:13.3	0:27:57.2	0:28:03.1	0:29:40.2	0:33:17.6	0:33:25.3	0:33:29.1
	MAHO 600E	HS	0:13:48.8	0:31:42.8	1:02:24.8	0:17:35.1	0:40:19.1	1:18:37.1	0:28:52.8	1:07:35.2	2:13:07.7
		FP	0:10:45.1	0:11:20.2	0:11:48.2	0:13:48.4	0:14:06.2	0:14:42.3	0:19:19.1	0:20:13.7	0:20:41.2
		ISO	0:12:20.3	0:12:55.3	0:13:18.7	0:19:20.1	0:19:30.1	0:19:46.5	0:21:19.7	0:21:34.5	0:22:25.1
		O-Grid	0:10:13.7	0:10:38.5	0:10:55.9	0:12:06.4	0:12:11.7	0:12:15.6	0:17:48.3	0:17:58.1	0:18:02.0
		$BSFC_H$	0:10:15.3	0:10:38.3	0:10:39.7	0:13:40.9	0:13:42.7	0:13:48.7	0:18:32.3	0:18:40.6	0:18:47.1
		$BSFC_O$	0:09:18.3	0:09:39.1	0:09:40.4	0:11:00.3	0:11:01.7	0:11:06.6	0:18:45.0	0:18:53.3	0:18:59.9
Advantage rel. to ISO	Toolpath Length (mm)	O-Grid	13.3%	14.6%	17.1%	19.0%	19.5%	20.8%	2.4%	3.1%	3.2%
		$BSFC_H$	20.3%	20.3%	20.9%	19.1%	20.1%	20.4%	7.7%	8.1%	8.2%
		$BSFC_O$	19.4%	19.4%	19.9%	24.7%	25.7%	26.0%	12.3%	12.8%	12.8%
	HAAS VF2TR	O-Grid	8.6%	9.1%	9.6%	23.3%	25.7%	27.3%	14.8%	15.1%	16.2%
		$BSFC_H$	14.1%	15.0%	16.6%	21.7%	24.6%	27.8%	20.9%	21.5%	22.5%
		$BSFC_O$	17.8%	18.7%	20.1%	23.8%	26.6%	29.8%	19.7%	20.3%	21.3%
	MAHO 600E	O-Grid	17.1%	17.6%	17.9%	37.4%	37.5%	38.0%	16.5%	16.7%	19.6%
		$BSFC_H$	16.9%	17.7%	19.9%	29.2%	29.7%	30.2%	13.1%	13.4%	16.2%
		$BSFC_O$	24.6%	25.3%	27.3%	43.1%	43.4%	43.8%	12.1%	12.5%	15.3%

Table 10 Molar, premolar and canine: CC points, kinematic error, ACT vs. ISO

			HAAS VF2TR			MAHO 600E		
Scallop height	**Method**	**Type**	**Molar**	**Premolar**	**Canine**	**Molar**	**Premolar**	**Canine**
0.065	**ISO**	N_{CC}	1645	788	342	379	203	58
		$\overline{\varepsilon}$	0.078	0.059	0.035	0.039	0.019	0.012
		σ_{ε}	0.170	0.173	0.065	0.048	0.074	0.033
	O-Grid	N_{CC}	1637	708	302	577	163	59
		$\overline{\varepsilon}$	0.073	0.064	0.041	0.038	0.024	0.012
		σ_{ε}	0.174	0.280	0.062	0.058	0.051	0.031
	$BSFC_H$	N_{CC}	1575	748	306	478	174	59
		$\overline{\varepsilon}$	0.069	0.060	0.035	0.038	0.021	0.012
		σ_{ε}	0.167	0.220	0.058	0.049	0.062	0.030
	$BSFC_O$	N_{CC}	1619	741	304	468	175	56
		$\overline{\varepsilon}$	0.068	0.057	0.033	0.036	0.021	0.011
		σ_{ε}	0.167	0.209	0.056	0.051	0.060	0.030
0.025	**ISO**	N_{CC}	3080	1654	984	776	445	171
		$\overline{\varepsilon}$	0.048	0.037	0.026	0.026	0.017	0.011
		σ_{ε}	0.143	0.163	0.059	0.046	0.065	0.018
	O-Grid	N_{CC}	3099	1655	920	1171	435	164
		$\overline{\varepsilon}$	0.042	0.037	0.028	0.026	0.017	0.010
		σ_{ε}	0.142	0.253	0.051	0.032	0.035	0.018
	$BSFC_H$	N_{CC}	2966	1638	933	974	427	159
		$\overline{\varepsilon}$	0.044	0.036	0.026	0.024	0.016	0.010
		σ_{ε}	0.128	0.202	0.053	0.035	0.048	0.016
	$BSFC_O$	N_{CC}	2957	1632	936	974	418	165
		$\overline{\varepsilon}$	0.040	0.036	0.026	0.024	0.017	0.009
		σ_{ε}	0.138	0.196	0.052	0.036	0.048	0.016
0.0125	**ISO**	N_{CC}	6359	3692	2115	1878	1206	520
		$\overline{\varepsilon}$	0.021	0.025	0.018	0.014	0.012	0.009
		σ_{ε}	0.130	0.183	0.048	0.042	0.057	0.016
	O-Grid	N_{CC}	6309	3698	2086	2897	1134	490
		$\overline{\varepsilon}$	0.021	0.024	0.018	0.015	0.012	0.008
		σ_{ε}	0.101	0.236	0.046	0.023	0.025	0.016
	$BSFC_H$	N_{CC}	6207	3621	2079	2292	1170	480
		$\overline{\varepsilon}$	0.019	0.025	0.017	0.014	0.012	0.008
		σ_{ε}	0.104	0.207	0.043	0.030	0.040	0.016
	$BSFC_O$	N_{CC}	6292	3597	2093	2261	1158	492
		$\overline{\varepsilon}$	0.019	0.024	0.017	0.013	0.011	0.008
		σ_{ε}	0.105	0.194	0.044	0.029	0.038	0.015

CONCLUSIONS

A new framework for generation of adaptive vector field aligned toolpaths for five-axis machining has been presented and analyzed. The method provides up to 70% decrease of the machining time with regard to the ISO toolpath, and up to 64% with regard to FP of NX9 (the best reference method). The advantages with regard to HS of NX9 and MasterCAM are overwhelming: the machining time is 10-20 times shorter. The tests against the benchmark toolpath generation show that the kinematic error and the roughness of the workpiece remain practically unchanged while the machining time, toolpath length, and waviness have been considerably reduced.

ACKNOWLEGEMENT

This research is supported by the Center of Excellency in Biomedical Engineering of Thammasat University and the National Research Council of Thailand (Grant No. 168974).

REFERENCES

1. C.C.Lo, Efficient cutter-path planning for five-axis surface machining with a flat-end cutter. *Computer-Aided Design.* **31**, 557-566, 1999.
2. A. Rao, R. Sarma, On local gouging in five-axis sculptured surface machining using flat-end tools. *Computer-Aided Design.* **32**, 409-420, 2000.
3. C.-J. Chiou, C-J, Y.-S. Lee, A machining potential field approach to tool path generation for multi-axis sculptured surface machining. *Computer-Aided Design*, **34,** 357-371, 2002.
4. W. Anotaipaiboon, S.S. Makhanov, E.L.J. Bohez, Optimal setup for five-axis machining. *International Journal of Machine Tools and Manufacture,* **46**, 964-977, 2006.
5. J. Gao, X. Chen, D. Zheng, O.Yilmaz, N. Gindy.Adaptive restoration of complex geometry parts through reverse engineering application. *Advances in Engineering Software.* **37**,592-600, 2006.
6. Y.-S. Lee, Admissible tool orientation control of gouging avoidance for 5-axis complex surface machining. *Computer-Aided Design*, **29**, 507-521, 1997.
7. W. Anotaipaiboon, S.S. Makhanov, Minimization of the kinematics error for five-axis machining. *Computer-Aided Design,* **43**, 1740-1757, 2011.
8. J.-H. Yoon, Tool tip gouging avoidance and optimal tool positioning for 5-axis sculptured surface machining. *International Journal of Production Research,* **41**, 2125-2142, 2003.
9. Y.-S. Lee, Non-isoparametric tool path planning by machining strip evaluation for 5-axis sculptured surface machining. *Computer-Aided Design*, **30**, 559-570. 1998.
10. Y.-S. Lee, Mathematical modelling using different endmills and tool placement problems for 4- and 5-axis NC complex surface machining. *International Journal of Production Research,* **36**, 785-814, 1998.
11. J. Dong, P.M. Ferreira, J.A. Stori, Feed-rate optimization with jerk constraints for generating minimum-time trajectories. *International Journal of Machine Tools and Manufacture*, **47**, 1941-1955, 2007.
12. T. Kim, S.E. Sarma, Toolpath generation along directions of maximum kinematic performance: a first cut at machine-optimal paths. *Computer-Aided Design,* **34**, 453-468, 2002.
13. C. My, E.L.J. Bohez, S.S. Makhanov, Critical point analysis of 3D vector field for 5-axis toolpath optimization. *Forth Asian Conference on Industrial Automation and Robotics, Bangkok, Thailand, 11-13 May, 2005.*

14. S.S. Makhanov, Optimization and correction of the tool path of the five-axis milling machine: Part 1. Spatial optimization. *Mathematics and Computers in Simulation*, **75**, 210-230, 2007.
15. L.L. Li, Y.F. Zhang, H.Y.Li, L. Geng, Generating tool-path with smooth posture change for five-axis sculptured surface machining based on cutter's accessibility map. *The International Journal of Advanced Manufacturing Technology*, **53**, 699-709, 2011.
16. S. Moodleah, S.S. Makhanov, 5-axis machining using a curvilinear tool path aligned with the direction of the maximum removal rate. *The International Journal of Advanced Manufacturing Technology*, **80**, 65-90, 2015.
17. E. Bohez, S.S. Makhanov, K. Sonthipermpoon, Adaptive nonlinear tool path optimization for five-axis machining. *International Journal of Production Research*, **38**, 4329-4343, 2000.
18. S.S. Makhanov, An application of variational grid generation techniques to the tool-path optimization of industrial milling robots, *Computational Mathematics and Mathematical Physics*, **39**, 1524–1535, 1999.
19. S. S. Makhanov, S.A.Ivanenko, Grid generation as applied to optimize cutting operations of the five-axis milling machine. *Applied Numerical Mathematics*, **46**, 331-351, 2003.
20. J.F. Thompson, B.K. Soni, N.P Weatherill, *Handbook of grid generation*. CRC Press, 1998.
21. S.A. Ivanenko, Generation of non-degenerate meshes. *Computational Mathematics and Mathematical Physics*, **28**, 141-146, 1998.
22. M.B Bieterman, D.R. Sandstrom, A curvilinear tool-path nethod for pocket machining. *Journal of Manufacturing Science and Engineering*, **125**, 709-715, 2003.
23. W. Anotaipaiboon, S.S. Makhanov. Toolpath generation for five-axis NC machining using space-filling curves, *The Third Asian Conference on Industrial Automation and Robotics*, Bangkok, Thailand, May 8-9, 2003.
24. W. Anotaipaiboon, S.S. Makhanov, Tool path generation for five-axis NC machining using adaptive space-filling curves. *International Journal of Production Research*, **43**, 1643-1665, 2005.
25. M.W. Bern, D. Eppstein, Quadrilateral meshing by circle packing. *International Journal Computational Geometry and Applications* **10**, 347-360, 2000.
26. P.J. Frey, P.-L. George, *Mesh Generation: Application to Finite Elements*, ISTE 2007.
27. 3D Systems Inc, Stereolithography Interface Specification. P/N 50065-S01-00, 1989.
28. The Initial Graphics Exchange Specification (IGES) Version 5.0. National Institute of Standards and Technology, Gaithersburg, MD, 1990.
29. ISO 10303-21:2002 Industrial automation systems and integration -- Product data representation and exchange -- Part 21: Implementation methods: Clear text encoding of the exchange structure, 2002.
30. Automatisation industrielle. Representation externe des donnees de definition de produits. Specification du standard d'echange et de transferts (SET), Version 85-08, Z68-300, Association Francaise de Normalisation (AFNOR) 85181, Paris. 1985.
31. http://en.wikipedia.org/wiki/CATIA, June 1, 2015.
32. http://en.wikipedia.org/wiki/PHIGS, June 1, 2015.
33. D.L. Marcum, J.A. Gaiter, Unstructured surface grid generation using global mapping and physical space approximation, *8th International Meshing Roundtable, CA, October 10-13, 1999.*
34. M. Eck, T. DeRose, T.Duchamp, H.Hoppe, M. Lounsbery, W. Stuetzle, Multiresolution analysis on arbitrary meshes. *The 22nd Annual Conference on Computer Graphics and Interactive Techniques*, Los Angeles,USA,August 06 - 11, 1995

35. M.S. Floater,Parametrization and smooth approximation of surface triangulations. *Computer Aided Geometric Design*, **14**, 231-250 (1997).
36. A. Sheffer, E.de Sturler, Parameterization of faceted surfaces for meshing using angle-based flattening, *Engineering with Computers.* **17**, 326-337, 2001.
37. J. McCartney, B.K. Hinds, B.L Seow, The flattening of triangulated surfaces incorporating darts and gussets, *Computer-Aided Design*, **31**, 249-260, 1999.
38. Y. Zhong, B. Xu, A physically based method for triangulated surface flattening. *Computer-Aided Design*, **38**, 1062-1073, 2006.
39. J. Xu, C. Jin, Boundary-conformed machining for trimmed free-form surfaces based on mesh mapping. *International Journal of Computer Integrated Manufacturing*, **26**, 720-730, 2013.
40. L. Saroul, Surface extraction and flattening for anatomical visualization. PhD. Thesis Université de Saint-Etienne, France, 2006.
41. http://www.resurf3d.com/MeshFlatten_standalone.htm (June 1, 2015).
42. S. Rusinkiewicz, Estimating curvatures and their derivatives on triangle meshes. *3D Data Processing, Visualization, and Transmission, 2nd International Symposium*, Tessaloniki, Greece, September 6-9, 2004.
43. P. Hu, K. Tang, Five-axis tool path generation based on machine-dependent potential field. *International Journal of Computer Integrated Manufacturing* (in print) DOI:101080/0951192X20151068451.
44. J.U. Brackbill, J.S. Saltzman, Adaptive zoning for singular problems in two dimensions. *Journal of Computational Physics.* **46**, 342-368, 1982.
45. J.E.Castillo, J.S. Otto, Numerical techniques for the transformation to an orthogonal coordinate system aligned with a vector field. *Computers & Mathematics with Applications.* **40**, 523-535, 2000.
46. A.E. Giannakopoulos, A.J. Engel, Directional control in grid generation. *Journal of Computational Physics*, **74**, 422-439, 1988.
47. S.S. Makhanov, W. Anotaipaiboon, *Advanced numerical methods to optimize cutting operations of five axis milling machines*. Springer, 2007.
48. M. Gaspar, F.Weichert, Integrated construction and simulation of tool paths for milling dental crowns and bridges. *Computer-Aided Design*, **45**, 1170-1181, 2013.
49. T.V. Vorburger, J. Raja, *Surface Finish Metrology Tutorial*. NISTIR 89-4088: National Institute of Standards and Technology, Gaithersburg, MD, June 1990.
50. A, Tabenkin, Function: the key to surface finish requirements. *4th Biennial International Manufacturing Technology Conference*, McLean, VA, 1988.
51. American National Standard. ASME/ANSI B46.1-1985. Surface Texture. American Society of Mechanical Engineers, 1985.
52. M.F. Siladic, Numerical grid generation and potential airfoil analysis and design. M.Sc. Thesis, The University of Texas of Austin, 1987.